GJI Geodynamics and tectonics

A unified continuum representation of post-seismic relaxation mechanisms: semi-analytic models of afterslip, poroelastic rebound and viscoelastic flow

Sylvain Barbot* and Yuri Fialko

*Institute of Geophysics and Planetary Physics, Scripps Institution of Oceanography, University of California San Diego, La Jolla, CA 92093-0225, USA.
E-mail: sbarbot@ucsd.edu*

SUMMARY

We present a unified continuum mechanics representation of the mechanisms believed to be commonly involved in post-seismic transients such as viscoelasticity, fault creep and poroelasticity. The time-dependent relaxation that follows an earthquake, or any other static stress perturbation, is considered in a framework of a generalized viscoelastoplastic rheology whereby some inelastic strain relaxes a physical quantity in the material. The relaxed quantity is the deviatoric stress in case of viscoelastic relaxation, the shear stress in case of creep on a fault plane and the trace of the stress tensor in case of poroelastic rebound. In this framework, the instantaneous velocity field satisfies the linear inhomogeneous Navier's equation with sources parametrized as equivalent body forces and surface tractions. We evaluate the velocity field using the Fourier-domain Green's function for an elastic half-space with surface buoyancy boundary condition. The accuracy of the proposed method is demonstrated by comparisons with finite-element simulations of viscoelastic relaxation following strike-slip and dip-slip ruptures for linear and power-law rheologies. We also present comparisons with analytic solutions for afterslip driven by coseismic stress changes. Finally, we demonstrate that the proposed method can be used to model time-dependent poroelastic rebound by adopting a viscoelastic rheology with bulk viscosity and work hardening. The proposed method allows one to model post-seismic transients that involve multiple mechanisms (afterslip, poroelastic rebound, ductile flow) with an account for the effects of gravity, non-linear rheologies and arbitrary spatial variations in inelastic properties of rocks (e.g. the effective viscosity, rate-and-state frictional parameters and poroelastic properties).

Key words: Numerical solutions; Dynamics and mechanics of faulting; Dynamics of lithosphere and mantle.

1 INTRODUCTION

Interpretations of the geodetic, seismologic and geologic observations of deformation due to active faults require models that take into account complex fault geometries, spatially variable mechanical properties of the Earth's crust and upper mantle, evolution of damage and friction and rheology of rocks below the brittle–ductile transition (Tse & Rice 1986; Scholz 1988,1998). Studies of post-seismic relaxation typically rely on models of fault afterslip (e.g. Perfettini & Avouac 2004,2007; Johnson *et al.* 2006; Freed *et al.* 2006; Hsu *et al.* 2006; Barbot *et al.* 2009a; Ergintav *et al.* 2009), viscoelastic relaxation (Pollitz *et al.* 2000; Freed & Bürgmann 2004; Barbot *et al.* 2008b) and poroelastic rebound (Peltzer *et al.* 1998; Masterlark & Wang 2002; Jonsson *et al.* 2003; Fialko 2004) to explain the observations.

Existing semi-analytic models of time-dependent 3-D viscoelastic deformation (Rundle 1982; Pollitz 1997; Smith & Sandwell 2004; Johnson *et al.* 2009) are limited to linear constitutive laws. Fully numerical methods (e.g. finite element) may be sufficiently versatile to incorporate laboratory-derived constitutive laws for ductile response (Reches *et al.* 1994; Freed & Bürgmann 2004; Parsons 2005; Freed *et al.* 2007; Pearse & Fialko 2010), but often require elaborate and time-consuming discretization of a computational domain, especially for non-planar and branching faults, and assignment of spatially variable material properties to different parts of a computational mesh. Another challenge arises from modelling of several interacting mechanisms (Masterlark & Wang 2002; Fialko 2004; Johnson *et al.* 2009). For example, geodetic data from the 1992 Landers, California, earthquake were used to argue for the occurrence of a poroelastic rebound, a viscoelastic flow in the lower crust and upper mantle, and afterslip on the down-dip extension of the main rupture, either individually or in various combinations (Peltzer *et al.* 1998; Deng *et al.* 1998; Freed & Bürgmann 2004;

---

*Now at: The Division of Geological and Planetary Sciences, California Institute of Technology, USA.
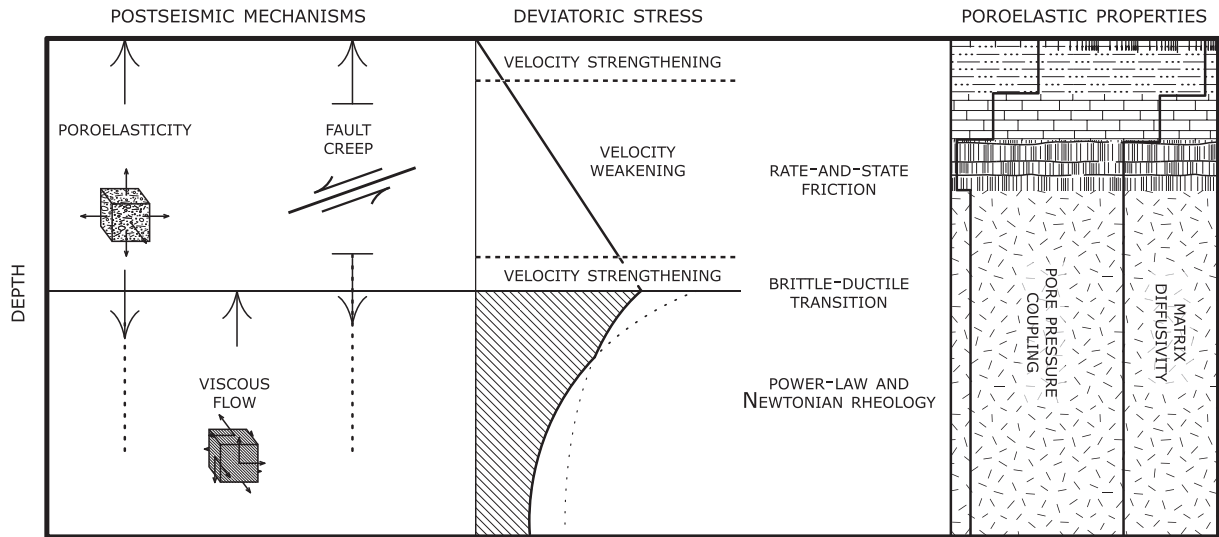
Figure 1. Sketch of inelastic properties of the lithosphere responsible for post-seismic transients. Post-seismic deformation may be due to a combination of poroelastic response, fault creep and viscous shear. The shear flow in the mantle and lower crust might be governed by a power-law viscosity for high stress and by a Newtonian viscosity at lower stress. In the former case, the effective viscosity is stress dependent. Afterslip on fault roots may be governed by a velocity-strengthening friction law. Poroelastic rebound can occur throughout the lithosphere but its effect likely decreases with increasing depth.

Fialko 2004; Perfettini & Avouac 2007). Data from the 2002 Denali earthquake were also shown to be broadly compatible with the occurrence of these three main mechanisms (e.g. Freed *et al.* 2006; Biggs *et al.* 2009; Johnson *et al.* 2009).

In this paper, we introduce a computationally efficient 3-D semi-analytic technique that obviates the need for custom-built meshes but is sufficiently general to handle complex fault geometries and non-linear rheologies. We develop a unified representation of the main mechanisms thought to participate in post-seismic relaxation (Fig. 1). The model employs a generalized viscoelastoplastic rheology that is compatible with linear and power-law viscous flow, poroelastic rebound and fault creep (afterslip). This framework allows one to construct fully coupled models that account for more than one mechanism of relaxation. In Section 2, we describe a general method to evaluate time-series of inelastic time-dependent relaxation. The approach is compatible with any non-linear rheology provided that the infinitesimal-strain approximation is applicable. We then consider particular cases of three dominant mechanisms of post-seismic relaxation. In Section 3 and Appendix A1, we introduce a special case of viscoelastic rheology equivalent to poroelasticity. In Section 4, we describe a viscoelastic rheology for fault creep with rate-strengthening friction. In Section 5, we consider Newtonian and power-law viscoelastic flow.

2 A UNIFIED REPRESENTATION OF POST-SEISMIC MECHANISMS: THEORY

Our method for evaluating 3-D time-dependent deformation due to earthquakes or magmatic unrest is based on a continuum representation of fault slip, viscous flow and change in pore fluid content. In this section, we describe the coupled equations that govern post-seismic deformation regardless of a particular relaxation mechanism and present a semi-analytic solution method to evaluate the time-series of relaxation. The proposed approach can accommodate different types of relaxation mechanisms and various degrees of strain localization in a medium.

In a generalized viscoelastic body Ω, with elastic compliance tensor D_{ijkl}, the total strain-rate tensor $\dot{\epsilon}_{ij}$ may be presented as the sum of elastic (reversible) and inelastic contributions

$$\dot{\epsilon}_{ij} = \dot{\epsilon}_{ij}^e + \dot{\epsilon}_{ij}^i, \tag{1}$$

where the dots represent time differentiation. In case of linear elasticity, the elastic strain-rate tensor can be written

$$\dot{\epsilon}_{ij}^e = D_{ijkl}\,\dot{\sigma}_{kl}, \tag{2}$$

where σ_{ij} is the Cauchy stress (Malvern 1969). The plastic strain rate $\dot{\epsilon}_{ij}^i$, also referred to as the eigenstrain rate, represents some relaxation process such as viscous flow, fault creep or poroelastic rebound. Any such source of time-dependent inelastic deformation contributes to a forcing term in strain space

$$\dot{\epsilon}_{ij}^i = \dot{\gamma} R_{ij}, \tag{3}$$

where γ is the amplitude of inelastic strain and R_{ij} is a unitary and symmetric tensor representing the local direction of the inelastic strain rate. The irreversible strain rate obeys a constitutive relationship or evolution law of the form

$$\dot{\gamma} = f(\sigma_{ij}, \gamma), \tag{4}$$

where σ_{ij} is the instantaneous Cauchy stress and γ is the cumulative amplitude of inelastic strain. Parameter γ in the evolution law (4) represents the effects of work strengthening (or softening). A particular form of operator f, which defines the material rheology, depends upon the relaxation mechanism. When no work hardening takes place the rheology $\dot{\gamma} = f(\sigma_{ij})$ is described by an algebraic equation. If the instantaneous inelastic strain rate depends on the history of deformation, then the rheology $\dot{\gamma} = f(\sigma_{ij}, \gamma)$ is described by a differential equation coupled to the equation for stress evolution. Poroelasticity, viscoelastic relaxation and fault creep can all be written in this general form.

Assuming infinitesimal strain, combining eqs (1)–(3) and integrating, we obtain the general hereditary equation for stress evolution

$$\sigma_{ij}(t) = C_{ijkl}\epsilon_{kl}(t) - \int_0^t \dot{\gamma} C_{ijkl} R_{kl}\mathrm{d}t, \tag{5}$$

where C_{ijkl} is the elastic moduli tensor. One interpretation of eq. (5) is that in a viscoelastic material the stress is reduced by a history

of inelastic relaxation. Notice that eq. (5) reduces to the Hooke's law at initial time ($t = 0$) and if no inelastic deformation occurs ($\dot{\gamma} = 0$). The total strain ϵ_{ij} can simply be evaluated from the current displacement field

$$\epsilon_{ij}(t) = \frac{1}{2}(u_{i,j} + u_{j,i}), \tag{6}$$

where the total displacement depends on a history of deformation,

$$u_i(t) = u_i(0) + \int_0^t v_i \, \mathrm{d}t, \tag{7}$$

v_i being the velocity field. Similarly, using eq. (1), the rate of change of stress, $\dot{\sigma}_{ij} = C_{ijkl}\dot{\epsilon}_{kl}^e$, can be written

$$\dot{\sigma}_{ij} = C_{ijkl}\left(\dot{\epsilon}_{kl} - \dot{\epsilon}_{kl}^i\right). \tag{8}$$

The inelastic contribution to the stress rate can be thought of as the instantaneous power density applied to body Ω by all internal processes, and as a forcing term in tensor space

$$\dot{m}_{ij} = C_{ijkl}\,\dot{\epsilon}_{kl}^i. \tag{9}$$

A time-dependent deformation at any point in Ω can be evaluated given a specific rheology (eq. 4). At all times, a displacement field must satisfy the condition of a vanishing total surface traction

$$\int_{\partial\Omega} \sigma_{ij}(t)\,\hat{n}_j \, \mathrm{d}A = 0, \qquad t \geq 0. \tag{10}$$

The criterion (10) is satisfied by enforcing simultaneously a free surface boundary condition $\dot{\sigma}_{ij}\hat{n}_j = 0$ and the equilibrium condition $\dot{\sigma}_{ij,j} = 0$. Using expressions (8) and (9) the free-surface boundary condition becomes

$$\dot{t}_i = C_{ijkl}\,\dot{\epsilon}_{kl}\,\hat{n}_j = \dot{m}_{ij}\hat{n}_j, \tag{11}$$

where $\hat{n}_i$ is the normal vector at the surface $\partial\Omega$. Eq. (11) indicates that a post-seismic source mechanism contributes to some equivalent rate of surface tractions $\dot{t}_i$ if the corresponding eigenstrain-rate $\dot{\epsilon}_{ij}^i$ is non-zero at the surface $\partial\Omega$. Without loss of generality, the equilibrium equation can be written

$$(C_{ijkl}\,\dot{\epsilon}_{kl})_{,j} + \dot{f}_i = 0. \tag{12}$$

Expression (12) reduces to the inhomogeneous Navier's equation in the case of a homogeneous isotropic elastic solid and we have defined the body-force rate as follows,

$$\dot{f}_i = -\dot{m}_{ij,j}. \tag{13}$$

The mechanisms driving a post-earthquake transient can be equivalently represented by an eigenstrain-rate (eq. 3), a power density (eq. 9) and a distribution of equivalent body force and surface traction rates (eqs 13 and 11, respectively). One important aspect of the proposed generalized viscoelastoplastic representation of post-seismic mechanisms is that regardless of a particular form of the constitutive relation, including non-linear relations, the instantaneous velocity field remains the solution to a linear partial differential equation. The velocity field satisfies the inhomogeneous Navier's equation (12) with the inhomogeneous boundary condition (11) and the methods used to solve elasto-static problems become applicable to evaluate models of non-linear time-dependent deformation.

The instantaneous velocity field v_i can in general be obtained with application of the elastic Green's function

$$v_i(x_i) = \int_\Omega G_{ij}(x_i, y_i)\,\dot{f}_j(y_i)\,\mathrm{d}V$$
$$+ \int_{\partial\Omega} G_{ij}(x_i, y_i)\,\dot{t}_j(y_i)\,\mathrm{d}A \tag{14}$$

or other numerical methods, for example using finite elements. Interestingly, the details of the geometry and the elastic structure of a viscoelastic body are all captured by the specific form of the elastic Green's function G_{ij}. The Green's function for a semi-infinite elastic solid is described by Love (1927) and Nemat-Nasser & Hori (1999). Because the equivalent body forces can be distributed over a large volume the convolution (14) can be computationally expensive. We alleviate this problem by using a Fourier-domain elastic Green's function which also accounts for a gravitational restoring force at the surface of the half space (Cochran *et al.* 2009; Barbot *et al.* 2008a, 2009b; Barbot & Fialko 2010).

A time-series of transient deformation following a stress perturbation can be obtained as follows. From a given level of stress at time t, we evaluate the eigenstrain rate due to a particular mechanism with eq. (3). We evaluate the corresponding power density (9) and compute the associated distribution of surface traction and internal forces with eq. (11) and (13), respectively. We then solve eq. (12) for a velocity field. We obtain the new displacement, stress, and cumulative strain fields for time $t + \mathrm{d}t$ by integrating the corresponding quantities in the time domain using an explicit method with a predictor/corrector scheme (Abramowitz & Stegun 1972). In particular, the stress-tensor field at $t + \mathrm{d}t$ is obtained from eq. (5). We repeat these steps until a simulation of the viscoelastic relaxation over a specified time interval is complete.

The method is sufficiently general to deal with most mechanisms believed to be relevant to post-seismic deformation such as Newtonian and non-Newtonian viscous flow, rate-strengthening fault creep and poroelasticity. One important advantage of the proposed method is its ability to handle arbitrary spatial variations in inelastic properties. Variations in inelastic properties are accounted for by changing the spatial distribution of the corresponding equivalent internal forces and surface tractions.

3 POROELASTIC REBOUND

The Earth's crust is a heterogeneous material composed of solid and fluid phases (e.g. porous rocks and pore fluids). The occurrence of a large earthquake alters the pore pressure in the crust. The induced stress change can create significant pore pressure gradients that may be relaxed by the movement of fluids if the host rocks are sufficiently permeable. The coupling between the pore–fluid diffusion and the effective stress introduces a time dependence into the response of the solid matrix (Biot 1941; Rice & Cleary 1976; Rudnicki 1985; Wang 2000; Coussy 2004). In this section, we present a viscoelastic rheology equivalent to poroelasticity. We demonstrate the equivalence between the equations of poroelasticity and the generalized viscoelasticity in Appendix A.

Using a formal decomposition of the strain rate tensor (eq. 1), we postulate that the inelastic strain involved in a poroelastic rebound is purely isotropic, that is the direction of relaxation in strain space is constant (cf. eq. 4)

$$R_{ij} = \frac{1}{3}\delta_{ij}, \tag{15}$$

where δ_{ij} is the Kronecker's delta. The poroelastic rebound thus can be viewed as an example of bulk viscosity. The amplitude of inelastic strain γ corresponds to the effective change in fluid content in the representative volume element (see eq. A11 in Appendix A). In the case of isotropic elastic properties, the amplitude of inelastic strain γ obeys the diffusive evolution law

$$\dot{\gamma} = D\left[(1 - \beta)\gamma - \beta\frac{\sigma}{\kappa_u}\right]_{,jj}, \tag{16}$$

Table 1. Example poroelastic moduli for common rocks.

Rock	K (GPa)	β	D (m^2 s^{-1})
Clay/mudstone	6	~1	10^{-1}
Sandstone/limestone	10	0.4	10^{-2}
Granite	40	0.25	10^{-5}
Basalt	40	0.03	10^{-5}

Note: Diffusivity values are for a fluid viscosity of $\mu = 10^{-3}$ Pa s and the bulk modulus is for undrained condition.

where κ_u is the undrained bulk modulus, $0 \le \beta \le 1$ is a non-dimensional parameter indicating the degree of coupling between the porous matrix and the pore space, $\sigma = \sigma_{kk}/3$ is the isotropic stress, positive for extension, and D is the diffusivity having units of length$^2 \times$time^{-1}. Eq. (16) is associated with the inhomogeneous surface boundary condition

$$\gamma = \frac{\beta}{1-\beta}\frac{\sigma}{\kappa_u}, \quad \text{at } x_3 = 0, \quad t > 0 \tag{17}$$

and the initial condition $\gamma = 0$ in Ω at $t = 0$. Notice that eq. (16) is of the form $\dot\gamma = f(\sigma_{ij}, \gamma)$, the general evolution law of a viscoelastic process. In its simplest, isotropic form, the poroelastic deformation requires only two additional parameters, compared to linear elasticity, to describe the post-seismic time-dependent deformation. The first parameter β is a non-dimensional coupling coefficient indicating what portion of the initial isotropic stress will eventually be relaxed. A material with $\beta \sim 1$ cannot sustain pressure gradients. The second parameter is the diffusivity D which controls the timescale of the relaxation. Appendix A gives relations between β, D and other commonly used poroelastic parameters. Typical values of macroscopic poroelastic parameters are shown in Table 1, using measurements from Detournay & Cheng (1993).

As fluid flow can take place in the entire crust, including near the surface, the equivalent-body-force representation of the poroelastic rebound seeks a proper distribution of internal forces and surface tractions. The power density, using eqs (9) and (15), becomes

$$\dot m_{ij} = \kappa_u \, \dot\gamma \, \delta_{ij} \tag{18}$$

and we obtain the corresponding internal force distribution per unit time

$$\dot f_i = -\kappa_u \, \dot\gamma_{,i} \tag{19}$$

associated with the surface-traction rate

$$\dot t_i = -\kappa_u \, \dot\gamma \, \delta_{i3}, \quad \text{at } x_3 = 0. \tag{20}$$

The instantaneous solid matrix velocity field can be obtained using eq. (14) with the forcing terms and traction boundary condition given by eqs (9) and (20), respectively. Time-series of poroelastic deformation can be generated using the approach developed in Section 2.

3.1 Computational schemes and benchmarks for poroelastic models

One complication of poroelastic models compared to the treatment of power-law viscosity, for example, is the evaluation of the evolution law. The presence of a Laplacian operator in the evolution law (16) makes an effective viscosity wavelength dependent. One simple way to evaluate the rate of fluid content is to use a finite-difference approximation. The finite difference method allows one to tackle heterogeneous properties and in particular to account for

vertical variations in fluid diffusivity D and matrix/pore coupling β. One important limitation, however, is the conditional stability of an explicit finite difference quadrature. The maximum time step of numerical integration is limited by the Courant condition (Press *et al.* 1992),

$$\Delta t_{\max} = \frac{\Delta x^2}{2\tilde D}, \tag{21}$$

where Δx is the grid sampling size and the product $\tilde D = (1 - \beta)D$ is taken to be the largest value in the computational domain. As the characteristic length scale of a problem is often a multiple of the sampling size, the finite-difference method often requires 50–100 computational steps to simulate a time interval of one characteristic relaxation-time. The full poroelastic rebound is approached only after several characteristic times so the finite-difference method poses a significant computational burden. Another approach to evaluate the rate of fluid content $\dot\gamma$ at time t_n is to perform the time integration in the Fourier domain. After Fourier transforming eq. (16) and assuming that the forcing term $\sigma(h)$ is in fact constant over a small time interval $[t_n, t_n + h]$, an approximation of the rate of fluid content is

$$\dot{\hat\gamma}(t_n + h) = -\tilde D\omega^2 e^{-\tilde D\omega^2 h}\left[\hat\gamma(t_n) - \frac{\beta}{1-\beta}\frac{\hat\sigma(t_n)}{\kappa_u}\right], \tag{22}$$

where $\omega = 2\pi(k_1^2 + k_2^2 + k_3^2)^{1/2}$ is the radial wavenumber and the hats denote the Fourier transform of the corresponding variables. If the assumption of a constant forcing term is satisfied then eq. (22) is an exact solution to the fluid diffusion partial differential equation (16). Our solution method for the diffusion equation coupled to the Navier's equation is as follows: For a given time step Δt, we evaluate analytically the fluid velocity at time $t_n + \Delta t/2$ in the Fourier domain using eq. (22). We then integrate the change in fluid content using a leapfrog quadrature in the space domain

$$\gamma(t_n + \Delta t) = \gamma(t_n) + \dot\gamma(t_n + \Delta t/2)\,\Delta t. \tag{23}$$

Naturally, the fluid velocity is also used to evaluate the coupled elastic deformation rate. The Fourier method of integration is unconditionally stable and small steps are required for accuracy only (to update the forcing term). We also use a predictor–corrector approach to march forward in time.

We test our viscoelastic formulation of the poroelastic equations with a simulation of the time-dependent poroelastic rebound following a strike-slip event. We first evaluate the full rebound using the difference between drained and undrained conditions. We then simulate the complete time-series of a poroelastic rebound and compare the fully-relaxed numerical solution to the analytic difference between drained and undrained solutions. The stress perturbation that is relaxed by poroelastic bulk viscosity in the crust is due to a strike-slip fault that extends from the surface to a depth of 1 km and has a uniform slip of 1 m. We choose Lamé parameters such that $\lambda_u = 1.5\,G$, where G is the shear modulus, and the coupling coefficient $\beta = 0.3$. The corresponding drained parameter is $\lambda_d = 0.85\,G$. We choose the diffusivity $D = 10^{-2}$ m^2 s^{-1}. The characteristic length scale is the depth of the fault $W = 1$ km which is associated with the diffusion timescale $t_m = W^2/2D = 1.6$ yr. Our simulation spans a time interval of $17\,t_m$, presumably enough to reach full relaxation. Fig. 2(a) (left panel) shows the initial displacement field at the surface due to the right-lateral strike-slip fault. The corresponding post-seismic displacement after complete fluid readjustment is shown in right panel of Fig. 2(a). We run two simulations, one using the finite difference method with a constant time step of $\Delta t = \Delta t_{\max}/5$, and another using the 'Fourier-leapfrog' method with adaptive time steps. Example displacement
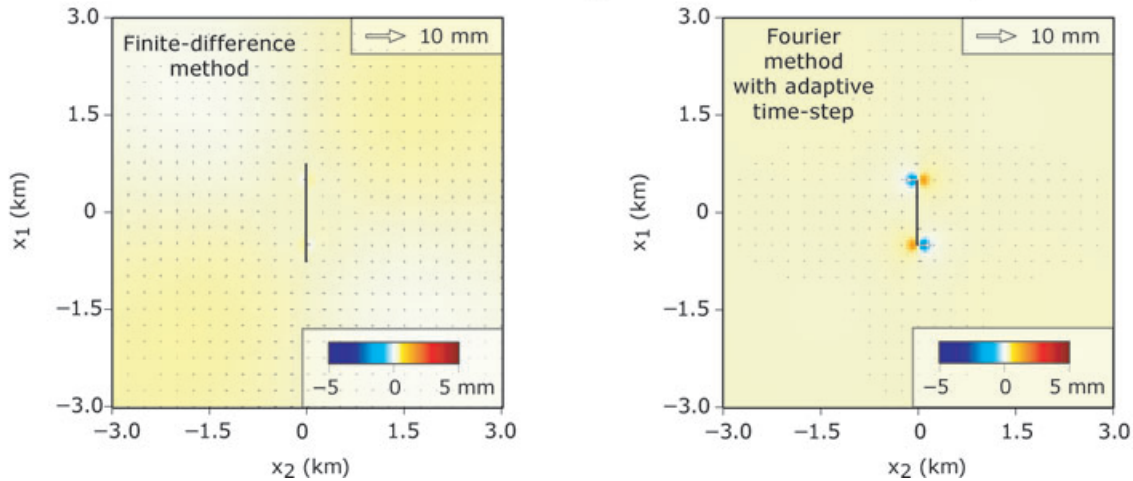
A. Strike-slip fault surface displacement and full poroelastic rebound (drained - undrained solutions)
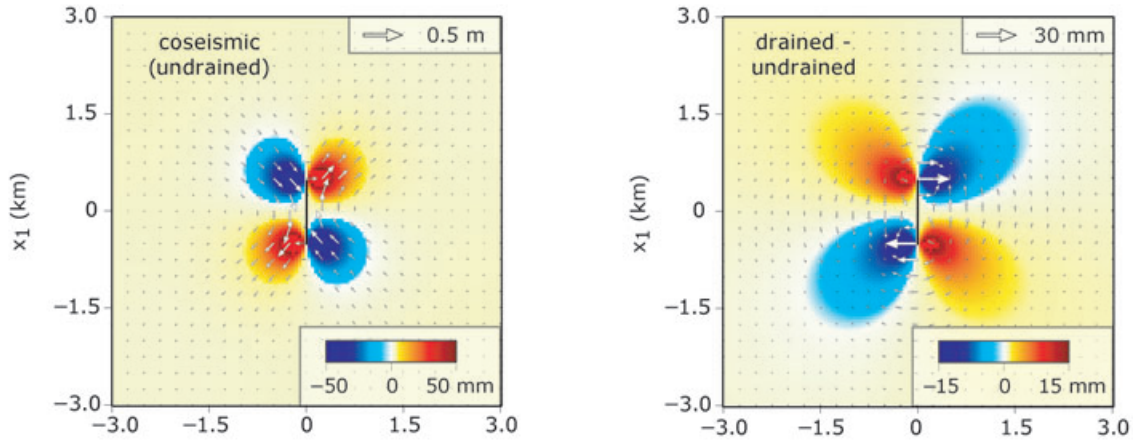
B. Snapshots of cumulative postseismic displacements before complete poroelastic rebound
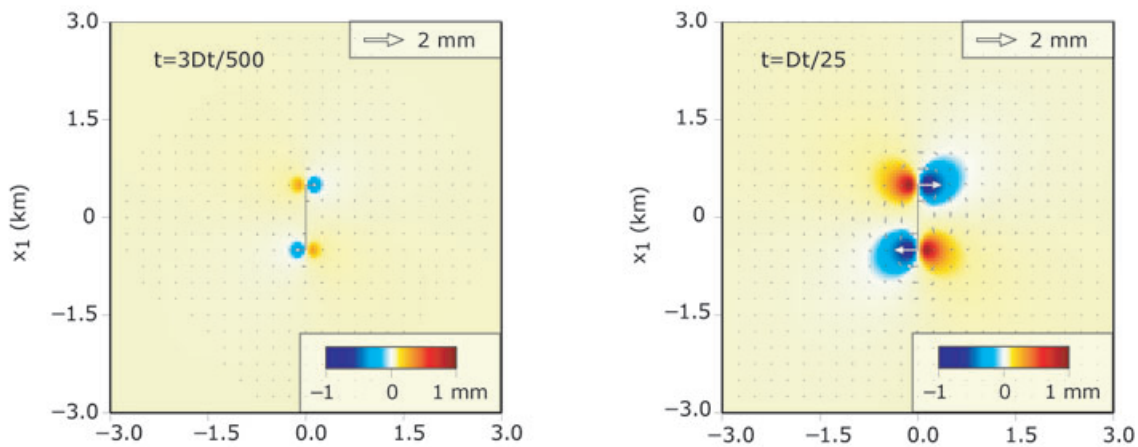
C. Residuals with finite-difference and Fourier time-integration methods at full relaxation (drained condition)

Figure 2. Benchmark for poroelastic rebound calculations. (a) The coseismic surface displacements due to a strike-slip fault slip (left panel) and post-seismic displacements due to a complete poroelastic rebound evaluated by taking the difference between the drained and undrained solution (right panel). (b) Example cumulative displacements before complete relaxation, illustrating an increase in amplitude and wavelength of deformation with time. (c) Comparison between our time-dependent calculations and the analytic solution at full relaxation (drained condition) for the case of a finite-difference (left panel) and a semi-analytic Fourier-domain integration method.

before full relaxation are shown in Fig. 2(b). The residuals between the finite-difference and 'drained-undrained' solutions at full rebound is shown in Fig. 2(c) (left panel). The residuals are characterized by long wavelengths which illustrates the well-known diffi-culty of resolving long wavelengths with a finite difference scheme for parabolic equations (Press *et al.* 1992). The residuals associ-ated with the Fourier-leapfrog method are shown in right panel of Fig. 2(c) and correspond to the last of the 130 steps required to reach
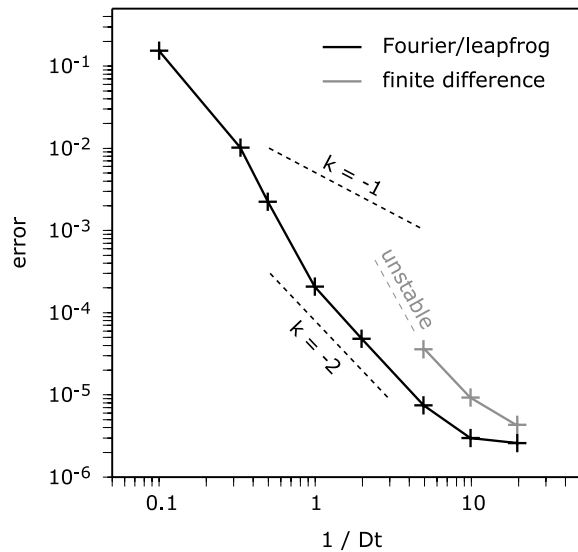
Figure 3. Efficiency diagram of the Fourier/leapfrog (black profile) and the finite difference (grey profile) integration schemes. The $k = -1$ and $k = -2$ slopes indicate the expected error reduction of second and third-order integration methods, respectively. The span of possible time steps is limited for the finite difference method due to a stability condition. The Fourier/leapfrog method is unconditionally stable and possible time steps cover at least three orders of magnitude with a consistent third-order convergence.

full rebound. The long wavelength displacement is much better resolved. Small short-wavelength residuals (Fig. 2c, right panel) are due to a continuum body force representation of a displacement discontinuity (Barbot *et al.* 2009b; Barbot & Fialko 2010), and depend on the grid size and the assumed tapering of slip on a fault.

Finally, we assess the accuracy of our proposed methods of time integration. Fig. 3 shows the efficiency diagram for the Fourier/leapfrog and the finite difference methods. We compute the L_2 norm of the error taken at time $t = 10\,t_{max}$ for various constant time-step sizes. The error is the norm of the difference between a given solution and a reference one which was obtained with an extremely small time step. Fig. 3 shows a cumulative error that decreases about quadratically with the step size for both methods. This large accuracy improvement with step size reduction indicates that the Fourier/leapfrog and the finite difference methods, when associated with a predictor–corrector approach, is third-order convergent. For a given reduced time step, the Fourier/leapfrog solutions are always about an order of magnitude more accurate than the finite difference counter part. The efficiency diagram 3 shows a range of possible time steps for the Fourier/leapfrog method covering about three orders of magnitude. The better accuracy of the Fourier/leapfrog method of integration along with the possibility of including adaptive time steps and a predictor/corrector scheme makes it much preferable over the finite-difference method.

4 FAULT CREEP

Fault creep, or aseismic sliding on a fault plane, is thought to be an important component of the earthquake cycle (e.g. Tse & Rice 1986). Afterslip has been widely documented following large earthquakes in various tectonic environments including subduction zones (Hsu *et al.* 2006) and transform faults (Bürgmann *et al.* 2002; Freed *et al.* 2006; Johnson *et al.* 2006; Barbot *et al.* 2009a). Recent studies show that afterslip can be the dominant mechanism responsible for post-seismic transients, at least in some locations (Freed 2007;

Barbot *et al.* 2009a), but it may also occur in combination with other mechanisms (Fialko 2004; Freed *et al.* 2006; Johnson *et al.* 2009). Laboratory experiments and modelling of geodetic data indicate that afterslip may be governed by a rate- and state-dependent friction (Marone *et al.* 1991; Marone 1998; Perfettini & Avouac 2007; Barbot *et al.* 2009a). In this section, we describe a continuum representation of rate-strengthening fault creep. We use the formulation of Barbot *et al.* (2009a) that regularizes the classic rate-and-state friction (Dieterich 1979, 1992) to allow for vanishing slip rates (Rice *et al.* 2001).

Fault creep can be viewed as a localized viscoelastoplastic deformation. The onset of sliding, or fault failure, is defined by the Coulomb yield stress (Byerlee 1978)

$$\tau - \mu\sigma, \tag{24}$$

where τ is the amplitude of shear traction in the direction of sliding, σ is the effective normal stress (positive for compression) accounting for the pore pressure contribution and μ is the coefficient of friction. A fault remains locked for strictly negative Coulomb stress $\tau < \mu\sigma$. In this case continuous loading causes deformation off of the fault (e.g. Heap *et al.* 2009). When shear stress is high enough, $\tau = \mu\sigma$, the fault fails and the subsequent slip evolution may be described by a rate-strenghtening friction rheology. Assuming small Coulomb stress before a stress perturbation, an assumption discussed in detail in (Barbot *et al.* 2009a), the slip rate is controlled by the local stress drop $\Delta\tau$ according to the constitutive law

$$\dot{s} = 2\dot{s}_0 \sinh\frac{\Delta\tau}{a\sigma}, \tag{25}$$

where $\dot{s}_0$ is a reference slip rate controlling the timescale of slip transients and $a\sigma$ is a parameter characterizing the effective stress and the degree of non-linearity in the afterslip evolution. Formulation (25) ignores the effect of a state variable evolution, which is justified if the slip speed changes sufficiently slowly.

To simulate fault creep in three dimensions, one needs to describe the geometry of the slip system. The change of traction t_i resolved on a fault surface S can be decomposed into normal and shear components,

$$t_i = \sigma_{ij}\hat{n}_j = t_k\hat{n}_k\,\hat{n}_i + \Delta\tau_i, \tag{26}$$

where $\hat{n}_i$ is the unit vector normal to the fault surface and $\Delta\tau_i$ is the shear component of the traction exerted on the fault such that $\Delta\tau = (\Delta\tau_k\Delta\tau_k)^{1/2}$. Noting the Burger vector of the dislocation $s_i = s\hat{s}_i$, we assume that the slip-rate vector is colinear with the direction of shear traction evaluated on the fault patch,

$$\dot{s}_i = \dot{s}\Delta\hat{\tau}_i \tag{27}$$

and the instantaneous inelastic strain-rate direction is (e.g. Nemat-Nasser 2004; Karato 2008)

$$R_{ij} = \frac{1}{2}(\Delta\hat{\tau}_i\hat{n}_j + \hat{n}_i\Delta\hat{\tau}_j). \tag{28}$$

In the continuum representation of fault creep, the slip rate $\dot{s}$ is associated with the inelastic strain rate

$$\dot{\gamma} = \dot{s}\,H_s(x_i), \tag{29}$$

where H_s, in dimensions of length^{-1}, is unity or zero according to whether its argument is or is not a point of the fault surface S. Fault representation using generalized functions is further discussed by Backus & Mulcahy (1976) and Barbot *et al.* (2009a). In this formulation, the rake of afterslip is governed by the local stress direction and slip is only constrained to occur on a predefined fault
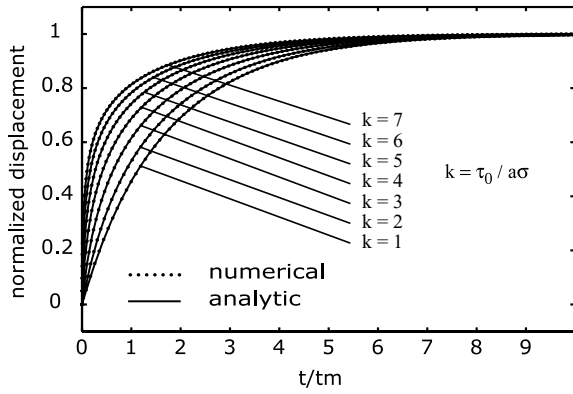
Figure 4. Benchmark for fault creep on a elementary fault segment (point source) governed by a rate-strengthening rheology. The Coulomb stress is perturbed homogeneously in the computational domain at time $t = 0$ with an amplitude τ_0. The responses of the fault as predicted by our numerical model and by the analytic solution to a spring-slider model are compared for various values of the initial stress perturbation. There is an excellent agreement between analytic and numerical solutions.

plane described by its position and orientation $\hat{n}_i$. Using eqs (28) and (29), the inelastic strain rate due to fault creep can be written $\dot{\epsilon}_{ij}^i = \dot{\gamma} R_{ij}$, mathematically analogous to other deformation mechanisms, so that our solution method described in Section 2 also applies in case of afterslip.

4.1 Benchmark of semi-analytic fault creep models

The response of a rate-strengthening point-source fault patch to a stress perturbation is described by Barbot *et al.* (2009a). The slip impulse response to a stress drop $\Delta\tau_0$ is

$$s(t) = \frac{\Delta\tau_0}{G^*}\left[1 - \frac{2}{k}\coth^{-1}\left(e^{t/t_0}\coth\frac{k}{2}\right)\right],\tag{30}$$

where G^* is the effective stiffness of the fault patch, the timescale of slip evolution is

$$t_0 = \frac{1}{2\dot{s}_0}\frac{a\sigma}{G^*}\tag{31}$$

and the degree of non-linearity of slip evolution is controlled by the dimensionless ratio

$$k = \frac{\Delta\tau_0}{a\sigma}.\tag{32}$$

We compare the predictions of afterslip for a point source using our generalized viscoelastic representation and the analytic solution (30). We consider the case of an elementary dislocation subjected to a stress drop $\Delta\tau_0$. We simulate the response of fault patches with frictional properties varying from $a\sigma = \Delta\tau_0/7$ to $a\sigma = \Delta\tau_0$. Fig. 4 shows a comparison between the numerical and analytic solutions. The numerical profiles represent the post-seismic displacements at the surface scaled by their maximum amplitude. We perform this comparison to remove a potential numerical bias due to the Fourier-domain elastic Green's function. Note an excellent agreement between analytic and numerical solutions for a wide range of stress perturbations (Fig. 4).

5 BULK DUCTILE FLOW

The lower-crust and upper-mantle rocks exhibit a ductile behaviour (Nur & Mavko 1974; Weertman & Weertman 1975; Brace &

Kohlstedt 1980; Karato & Wu 1993; Savage 2000) that is often invoked to explain large-wavelength post-earthquake deformation transients (Reilinger 1986; Pollitz *et al.* 2000; Johnson *et al.* 2009). Geodetic (Freed & Bürgmann 2004) and laboratory (Karato *et al.* 1986; Kirby & Kronenberg 1987; Kohlstedt *et al.* 1995) observations indicate a stress-dependent mantle viscosity, and suggest that a power-law rheology of the form

$$\dot{\epsilon}_{ij}^i = \dot{\gamma}_0\left(\frac{\tau}{G}\right)^{n-1}\frac{1}{G}\sigma_{ij}'\tag{33}$$

may be applicable to the lower crust and upper mantle, where $1 \leq n < 5$ is a power exponent, G is the shear modulus,

$$\sigma_{ij}' = \sigma_{ij} - \delta_{ij}\frac{\sigma_{kk}}{3}\tag{34}$$

is the deviatoric stress tensor and

$$\tau = \left(\frac{1}{2}\sigma_{kl}'\sigma_{kl}'\right)^{1/2}\tag{35}$$

is the norm of the deviatoric stress. The case of $n = 1$ corresponds to linear viscoelasticity. The strain-rate direction is purely deviatoric

$$R_{ij} = \frac{\sigma_{ij}'}{\tau}\tag{36}$$

and the constitutive law for strain rate is

$$\dot{\gamma} = \dot{\gamma}_0\left(\frac{\tau}{G}\right)^n,\tag{37}$$

where $\dot{\gamma}_0$ is a reference strain rate. Power-law creep is a thermally-activated process (Karato 2008) and $\dot{\gamma}_0$ is assumed to increase as a function of depth. For power exponent greater than unity the effective viscosity

$$\eta = \frac{1}{\dot{\gamma}_0}G^n\tau^{1-n}\tag{38}$$

is lower at the initial stage of a transient deformation when stress is higher. The ductile flow is not limited by a yield surface and for a constant stress condition the effective viscosity η increases exponentially with decreasing temperature (e.g. Karato 2008). A timescale of a post-seismic transient due to viscoelastic relaxation

$$t_m = \frac{\eta}{G} = \frac{1}{\dot{\gamma}_0}\left(\frac{G}{\tau}\right)^{n-1}\tag{39}$$

is stress dependent and is shorter near the onset than at the later stages of the transient. A ductile flow is thought to occur below the seismogenic zone (at depths greater than 15–50 km for a typical continental crust). The confinement of the flow below an elastic plate obviates the need for any equivalent surface traction ($\dot{t}_i = 0$) and the deformation can be represented by a distribution of internal forces only.

5.1 Numerical examples and benchmarks for viscoelastic models

We test our formulation of the power-law viscoelastic relaxation by considering the cases of stress perturbations due to strike-slip and dip-slip faults. In these test models, the fault slip occurs in an elastic plate that rests on a power-law viscoelastic half-space. Here, we ignore the effect of gravity. We compare the predictions of post-seismic displacement from our semi-analytic method with those computed using a finite-element approach. We use the commercial finite element software Simulia (formerly Abaqus, *www.simulia.com*) to perform the finite-element calculations.

A. Strike-Slip Fault. Power-law viscosity (n=3.5). Displacements and residuals with finite-element calculations
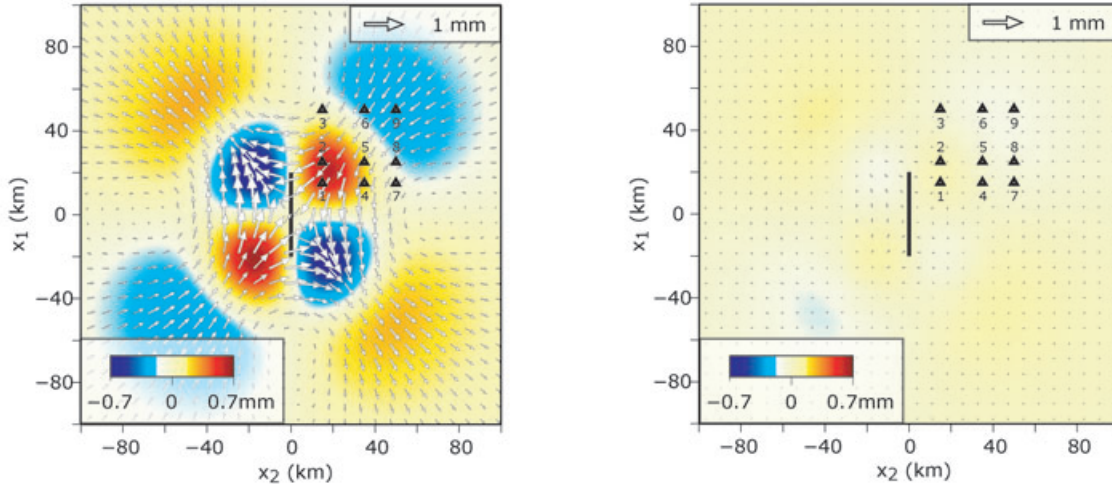
B. Comparison between finite-element and Fourier-domain postseismic time series
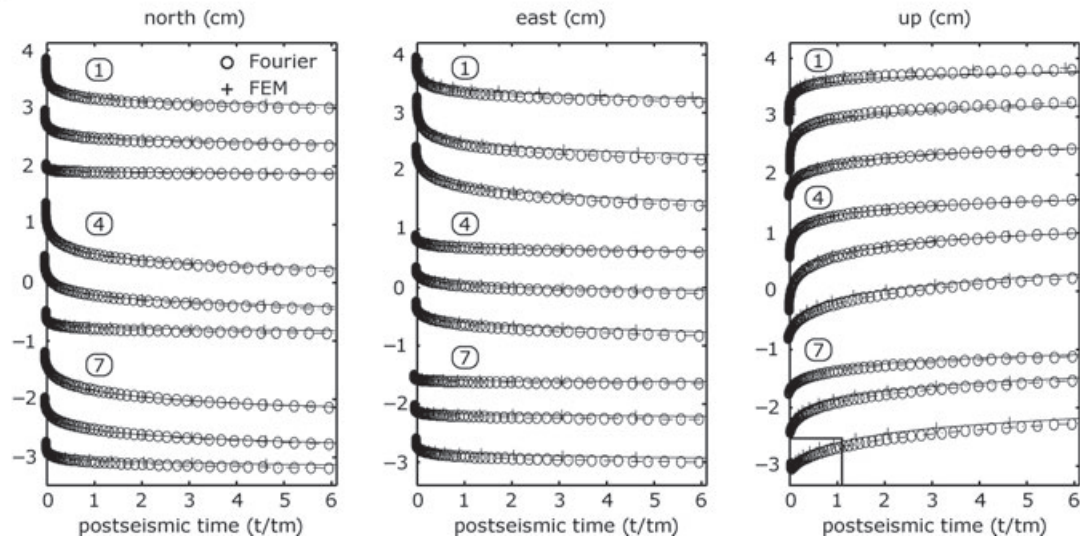
Figure 5. Calculated time-series of surface displacements due to as a stress perturbation in an elastic plate over a non-linear viscoelastic half-space. A vertical right-lateral strike-slip fault 40 km long extending from the surface to a depth of $L = 10$ km slips $s = 1$ m. The brittle–ductile transition occurs at a depth of 30 km. The post-seismic flow is governed by a power-law rheology with stress exponent $n = 3.5$. Elastic properties are uniform with $\nu = 1/4$. (a) A map view of post-seismic surface displacements at the early stage of the transient. The right panel shows difference between our solution and finite-element (FEM) calculations. (b) Time-series of surface displacements for an array of locations numbered from 1 to 9 in the corresponding map. Time is scaled by $t_m = \dot{\gamma}_0^{-1} s^{1-n} L^{n-1}$. The smaller time steps near the onset of the post-seismic transient are due to the adaptive time-step procedure. Notice a change of polarity of vertical displacement for point 9. The residuals between results from our numerical approach and the finite element calculation are less than 10 per cent and show reasonable agreement both in map view and in time.

5.1.1 Strike-slip fault models

We start with the case of a strike-slip fault in an elastic brittle layer. We assume uniform and isotropic elastic properties for a Poisson's solid (the Lamé parameters are such that $\lambda = G$ and Poisson's ratio is $\nu = 1/4$). The brittle–ductile transition is assumed at a depth of 30 km. Below 30 km, we assume a power-law rheology with a power exponent $n = 3.5$ (eq. 33). The fault slips 1 m uniformly from the surface to a depth of 10 km and is 40 km long. We perform a simulation of the viscoelastic post-seismic relaxation using our generalized viscoelastic formulation. We perform the computation on a $512^3 \sim 1.3 \times 10^8$ node grid with a uniform spacing between the nodes of $\Delta x_i = 0.8$ km. We use an explicit method to integrate velocity and stress. We choose the adaptive time step corresponding to

one tenth of the characteristic time suggested by eq. (39) and march forward in time using a second-order accurate predictor/corrector method. A snapshot of the post-earthquake surface displacement at early stage of the transient is shown in Fig. 5(a). For the respective finite-element calculation we use a 628332-node mesh with a sampling size going from 0.8 km near the fault to 11.5 km in the far field. We pin the boundary of the mesh 300 km away from the fault centre. Despite a considerably smaller number of nodes, the finite-element calculation took 2 weeks on an eight-node shared memory computer. The same simulation with the Fourier-domain method required 2 days of computation on the same machine.

A map view of the surface residuals between the simulations using our formulation and the ones using the finite element method is shown in the right panel of Fig. 5(a). The maximum discrepancy

between the two solutions is lower than 10 per cent. The simulated time-series of surface displacement at the points numbered from 1 to 9 is shown in Fig. 5(b). We choose to non-dimensionalize time with the reference time

$$t_m = \frac{1}{\dot{\gamma}_0} \left(\frac{s}{L} \right)^{1-n},$$ (40)

where $\dot{\gamma}_0$ and n are the reference strain rate and power exponent of the power law, respectively, and s/L is the strain drop on the fault. We use $s = 1$ m and $L = 10$ km. The time series exhibit the typical higher velocities near the onset of the post-seismic transient with rapidly decaying velocities at later times. There is an excellent agreement between results obtained using the finite element model and our method. A distinct feature of the power-law relaxation is a change of polarity of vertical displacements at the surface of the half- space. The change of polarity can be seen in the time-series of vertical displacement of far-field point number 9 in Fig. 5(b).

We perform another similar simulation using a Newtonian viscosity, that is with $n = 1$ in eq. (33), all other parameters being the same. A snapshot of the surface displacement due to the viscoelastic relaxation is shown in left panel of Fig. 6(a), corresponding to a time $t = 2t_m$ after the coseismic stress perturbation. The residuals with the finite-element forward model at this time is shown in left panel of Fig. 6(a). There is an excellent agreement between the finite-element and the semi-analytic results: the maximum residuals are less than 5 per cent of the expected signal. In Fig. 6(b), we compare the simulated time-series of viscoelastic relaxation at points numbered from 1 to 12 in Fig. 6(a). The distribution of sample points covers near- and far-field from the fault. The finite-element and Fourier time-series differ less than 5 per cent throughout a time interval spanning 12 characteristic relaxation times. The non-Newtonian and linear viscosity models converge to the same fully relaxed solution. Before the relaxation is complete, the post-seismic displacements due to a linear and a power-law rheology have the same polarity in the near field. In the far-field, however, the power-law relaxation due to slip of a vertical strike-slip fault has an opposite polarity compared to the Maxwell rheology. Our simulations indicate that the far-field post-seismic displacements due to a power-law mantle flow (with $n > 1$) change polarity early in the post-seismic transient.

5.1.2 Dip-slip fault models

We proceed with the evaluation of post-seismic relaxation due to dip-slip faulting. For simplicity, we consider the case of a vertical dip-slip fault with the same geometry as in the strike-slip models. Although the geometry is similar, dip-slip and strike-slip faults lead to very different stress changes in the surrounding rocks. We consider first the case of a non-linear viscoelastic upper mantle governed by the power-law rheology (eq. 33) with $n = 2$. A snapshot of the surface displacement early in the post-seismic transient is shown in Fig. 7(a). The vertical post-seismic displacement has the same polarity as the coseismic displacement. Horizontal post-seismic displacements, however, are opposite to the coseismic ones. We performed the same simulation using finite elements and the residuals are shown in the right panel of Fig. 7(a). There is an excellent agreement between the semi-analytic and the finite-element results. The time-series of surface post-seismic displacements at points numbered from 1 to 8 in the maps are shown in Fig. 7(b). There is an excellent agreement between the semi-analytic and the finite-element results. The time-series reveal two noteworthy features. First, the initial post-seismic velocities are much higher than at later times, as most visible for points 1 and 2. Secondly, a change in polarity occurs at far-field locations. The change of post-seismic displacement orientation is

most conspicuous for point 6 in the east–west direction. A subtle change of polarity can be misleadingly interpreted as a delayed post-seismic transient (e.g. see vertical displacement of point 8).

Finally, we consider the case of a dip-slip fault in an elastic plate over a Newtonian viscoelastic half-space. The geometry of the problem is the same as in previous models. The predictions from our semi-analytic model and the residuals with finite-element calculations at post-seismic time $t = t_m/2$ are shown in Fig. 8(a). The time-series of post-seismic displacement at surface positions in the near and far-field are shown in Fig. 8(b). There is an excellent agreement between the semi-analytic and the fully numerical solutions. Notice a change of polarity of far-field points 8 and 12. The overall patterns of surface displacement due to Newtonian and power-law viscosity are similar, in contrast to the case of a strike-slip fault. The overall agreement between the finite-element and the semi-analytic calculations suggests that our formulation is robust and can be used to model post-seismic deformation due to non-linear viscoelasticity.

The semi-analytic Fourier-domain equivalent body-force method vastly outperforms the finite element method for the same number of nodes, and remains computationally efficient even when the number of degrees of freedom is a few orders of magnitude larger than in a respective finite element model. The finite element method has the advantage of using meshes with variable spatial discretization. The Fourier method requires a uniform grid spacing, so a comparable resolution in an area of interest entails a larger problem size. Also, the periodic boundary conditions used in the Fourier method require the dimensions of the computation domain to be sufficiently large. This further increases the problem size. However, to a large extent this is compensated by a better computational efficiency. An appealing feature of the proposed method is that it does not require generation of complicated meshes, which itself can be an involved and time-consuming process, especially for complex fault geometries.

5.2 Effect of gravity on viscous relaxation

We include gravity in our model as the former may affect surface deformation in case of viscoelastic relaxation. The principal effect of gravity is to reduce the amplitude of large-wavelength vertical deformation at late stages of relaxation (Pollitz *et al.* 2000; Freed *et al.* 2007). To validate our approach, we reproduce the viscoelastic relaxation benchmarks of (Rundle 1982, Figs 6 and 7) and (Pollitz 1997, Fig. 3). The model includes a thrust fault buried in an elastic plate overlying a Newtonian viscoelastic half-space with uniform elastic properties. Poisson's ratio $\nu = 1/4$ is constant in the entire half-space. The brittle–ductile transition occurs at depth H. We assume a uniform density $\rho = 3300$ km m^{-3} in the half-space. The model of Rundle (1982) and Pollitz (1997) differs slightly in that they have an additional small density contrast at the brittle–ductile transition. The fault is dipping $30°$, is $20H/3$ long in the strike direction and H wide in the dip direction and U is the amplitude of slip. The magnitude of the gravitational restoring force is controlled by the buoyancy wavenumber (Barbot & Fialko 2010)

$$\Gamma = (1 - \nu) \frac{\Delta \rho g}{G},$$ (41)

where $\Delta \rho$ is the density contrast at the surface (i.e. between rock and air) and g is the acceleration of gravity.

Fig. 9(a) shows the simulated across-fault profiles of co- and post-seismic vertical component of displacements corresponding to the case of no gravity. The post-seismic vertical displacement after 45 relaxation times, close to the full relaxation, has higher

A. Strike-Slip. Linear viscoelasticity. Surface displacements and residuals with finite-element calculations
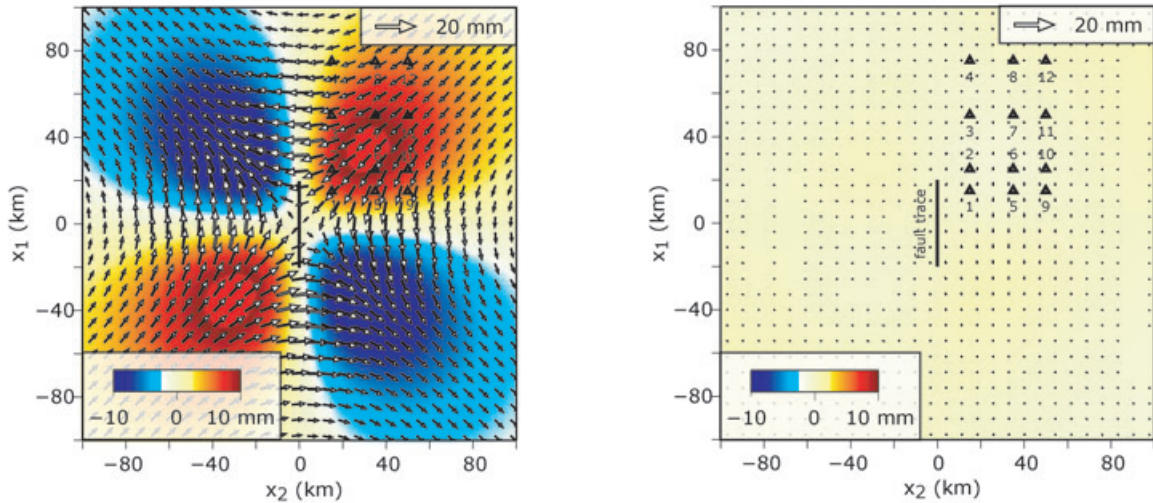
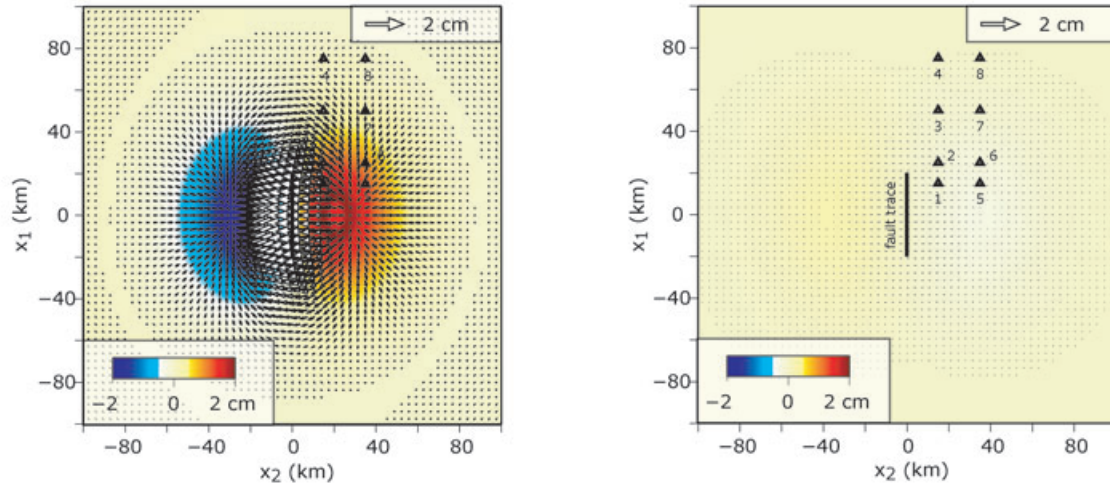**B. Comparison between finite-element and Fourier-domain postseismic time series**
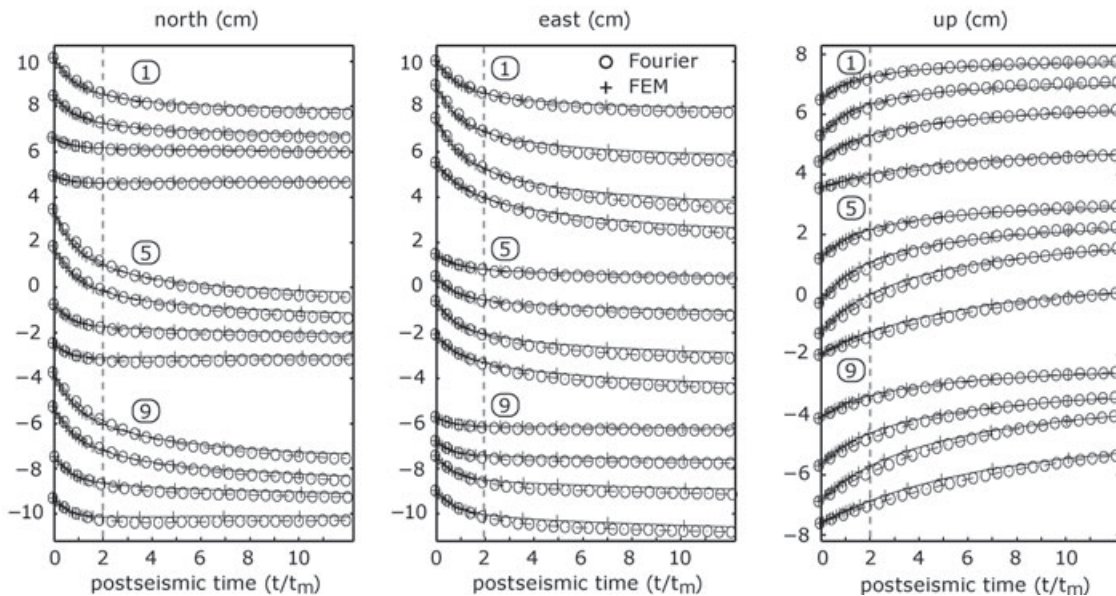
Figure 6. Calculated time-series of surface displacement for a model shown in Fig. 5, but for a linear viscoelastic layer (eq. 33 with $n = 1$). (a) Left panel: snapshot of post-seismic surface displacements at time $t = 2t_m$. Right panel: difference between our solution and a calculation using a finite element method (FEM). (b) Time-series of surface displacements for the points numbered from 1 to 9 in the corresponding map. Time is scaled by the Maxwell time $t_m = 1/\dot{\gamma}$. The maximum discrepancy between results from our numerical approach and the finite element calculation are less than 10 per cent.

amplitude and larger wavelength than the vertical displacement after just five relaxation times. Notice a few areas, for example between $x_2 = -4H$ and $x_2 = -2H$, that exhibit a reversal in the course of the post-seismic transient. Such a change of polarity is an expected feature of the post-seismic transient following a thrust fault, as shown by Rundle (1982) and Pollitz (1997). Our results indicate that it is typical of dip-slip faults, in general, for both linear and power-law rheologies (Figs 7 and 8). The corresponding simulations which include the effect of gravity are shown in Fig. 9(b). The early post-seismic displacement profile after five relaxation times is less affected by the gravitational restoring force. At later times, close to full relaxation, the vertical displacement is reduced by about a factor of two compared to the non-gravitational solution. The effect of buoyancy is more pronounced at later times when surface displacements have a larger wavelength. Results of Fig. 9

compare well with the simulations of Rundle (1982) and Pollitz (1997) despite our neglect of a density contrast at the brittle–ductile transition. The density contrast at the brittle–ductile transition has a much smaller effect on the patterns of surface displacements due to the smaller density contrast and the smaller wavelength of deformation at the fault tip. Our results confirm the conclusions of Rundle (1982) and Pollitz (1997) regarding a substantial effect of gravity on post-seismic displacements during late stages of viscoelastic relaxation.

6 CONCLUSIONS

We have introduced a unified representation of the main mechanisms believed to be involved in post-seismic transients. We showed that fault creep, pore fluid diffusion and viscous flow can all be

A. Dip-Slip Fault. Powerlaw viscoelasticity (n=2). Displacements and residuals with finite-element calculations

B. Comparison between finite-element and Fourier-domain postseismic time series
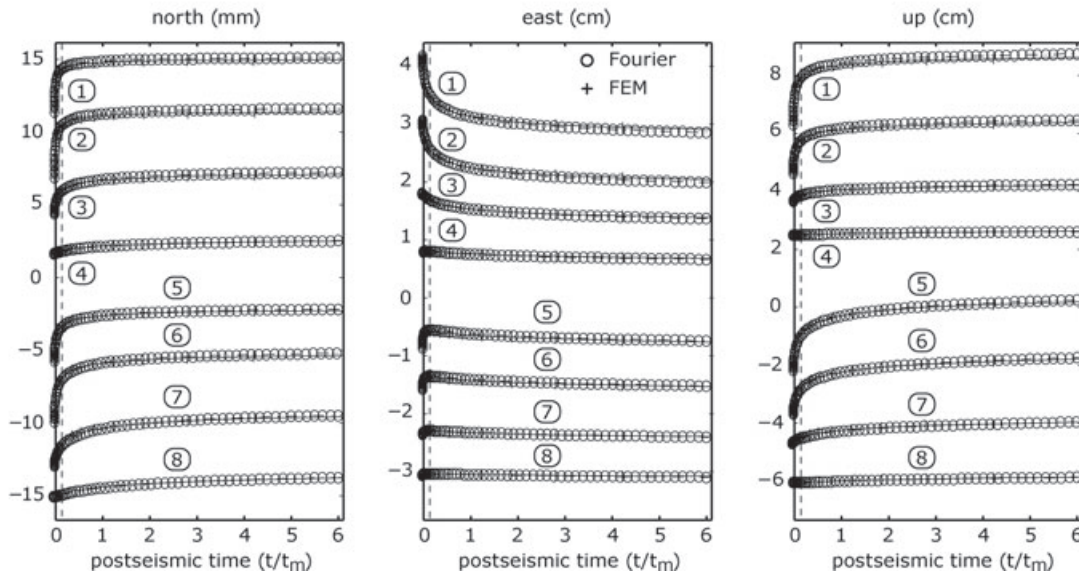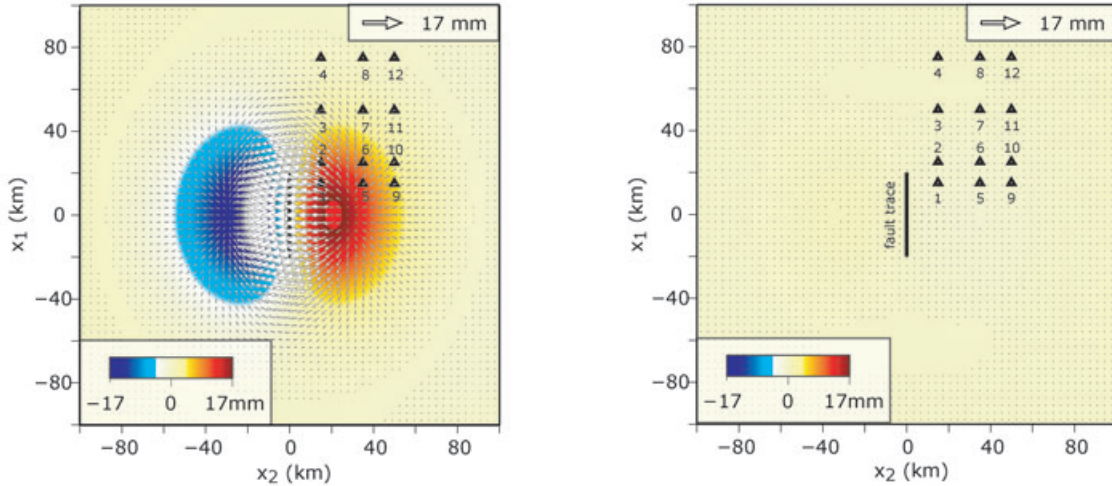

Figure 7. Benchmark for time-series of surface displacement due to a stress perturbation caused by a dip-slip fault in an elastic plate overriding a non-linear viscoelastic half-space. A vertical dip-slip fault 40 km long extending from the surface to a depth of 10 km slips 1 m. The brittle–ductile transition occurs at a depth of 30 km. The post-seismic flow is governed by a power-law rheology with stress exponent $n = 2.0$. Elastic properties are uniform with $\nu = 1/4$. (a) A map view of post-seismic surface displacements after 10 months. A similar computation is performed using finite elements with Abaqus and the residuals are shown in the right panel. (b) Time-series of surface displacements for the points numbered from 1 to 8 in the corresponding map. The smaller time steps near the onset of the post-seismic transient are due to the adaptative time-step procedure. Results from our approach are shown every five computation steps for clarity. The residuals between results from our numerical approach and the finite element calculation are less than 5 per cent and show reasonable agreement both in map view and in time.

formalized within a framework of a generalized viscoelastoplastic rheology. Each mechanism contributes to some inelastic strain to relax a certain quantity in the deformed body. The relaxed quantity is the deviatoric stress in case of viscoelastic relaxation, the shear stress in case of fault creep and the trace of the stress tensor in the case of poroelastic rebound. The proposed unified representation allows us to employ the same solution method to model post-seismic relaxation invoking the above mechanisms, for various rheologies (including non-linear ones) and allowing for interactions between different mechanisms.

Our approach to model post-seismic relaxation is to identify the power density that represents the effect of all driving mechanisms. The power density is associated with a distribution of internal forces

and surface tractions and the instantaneous velocity field is a solution to the inhomogeneous Navier's equation. The technique can handle non-linear rheologies because in this framework the instantaneous velocity satisfies a linear partial differential equation and all the strategies available to solve elastostatic problems are directly applicable. We solve for a velocity field semi-analytically using the Fourier-domain Green's function described in the companion paper (Barbot & Fialko 2010). In general, other Green's functions (i.e. designed for different boundary conditions, geometry or elastic properties) and other numerical methods can be used in conjunction with our body-force method. The Green's function of Barbot & Fialko (2010) corresponds to a uniform elastic half-space with a buoyancy boundary condition at the surface.

A. Dip-Slip Fault. Linear viscoelasticity. Surface displacements and residuals with finite-element calculations

B. Comparison between finite-element and Fourier-domain postseismic time series
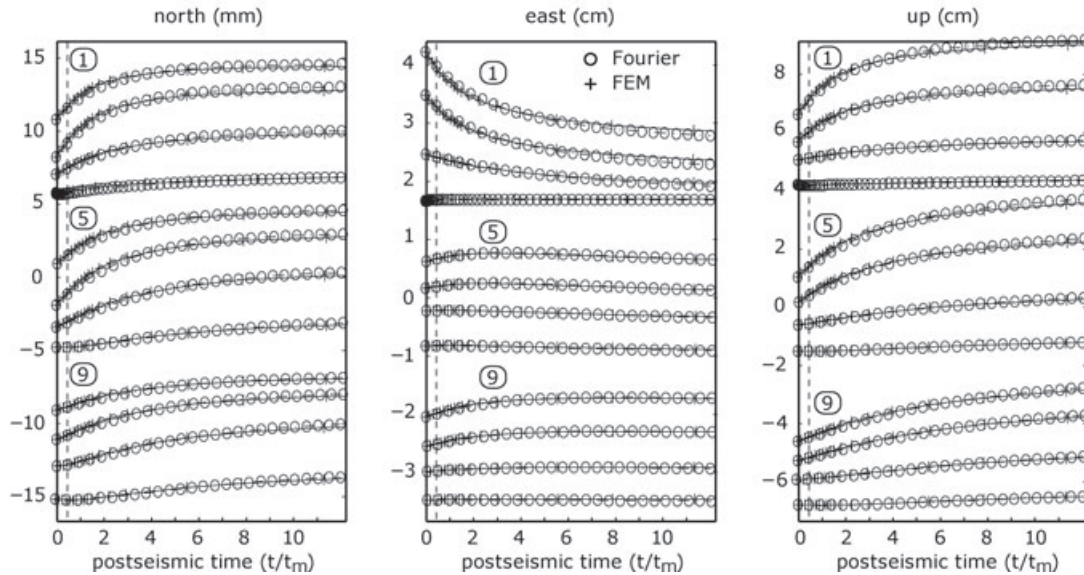

Figure 8. Benchmark for time-series of surface displacement following the rupture of a fault in an elastic plate over a linear viscoelastic layer. A vertical dip-slip fault 40 km long extending from the surface to a depth of 10 km slips 1 m. The brittle–ductile transition is 30 km deep. The post-seismic flow is governed by a linear viscoelastic rheology (eq. (33) with $n = 1$). Elastic properties are uniform with $\nu = 1/4$. (a) A snapshot of post-seismic surface displacements at time $t = 0.5t_m$. A similar computation is performed using finite elements with Abaqus and the residuals are shown in the right panel. (b) Time-series of surface displacements for the points numbered from 1 to 9 in the corresponding map. Results from our approach are shown every five computation steps. The maximum discrepancy between results from our numerical approach and the finite element calculation are less than 5 per cent.

We applied the method to model non-linear viscoelastic relaxation, stress-driven afterslip, an poroelastic rebound. We described the effect of pore fluid diffusion in a permeable medium in terms of an effective bulk viscous rheology whereby pressure is relaxed by changes in volumetric inelastic strain. We showed an equivalence between our bulk viscosity formulation and the classic theory of poroelasticity. In the bulk viscosity formulation of poroelasticity, the inelastic strain corresponds to an effective change in pore fluid content and obeys an inhomogeneous parabolic differential equation. We propose two solutions methods to evaluate the instantaneous strain rate due to pore-pressure diffusion. We successfully benchmarked our time-dependent simulations of poroelastic rebound against fully-relaxed solutions. We also showed a good agreement between our semi-analytic models of stress-driven fault creep and analytic solutions. Finally, we compared our simulations

to results of finite element calculations for cases of a Newtonian viscosity and a power-law rheology (with a stress power exponent of $n = 3.5$ and $n = 2$ for strike-slip and dip-slip faults, respectively). For all scenarios considered, we find a reasonable agreement between our semi-analytic solutions and the fully numerical results. We show that if the ductile flow is governed by a power-law rheology the transient deformation exhibits higher rates of deformation immediately following an earthquake. The onset of the power-law viscoelastic relaxation following slip on a strike-slip fault is also characterized by a change of polarity of vertical displacements in the far-field. The effect of gravity can be substantial at late stages of viscoelastic relaxation because of large-wavelength vertical displacements.

Our unified representation of post-seismic mechanisms enables sophisticated simulations of post-seismic relaxation that

A. Thrust fault - Viscoelastic
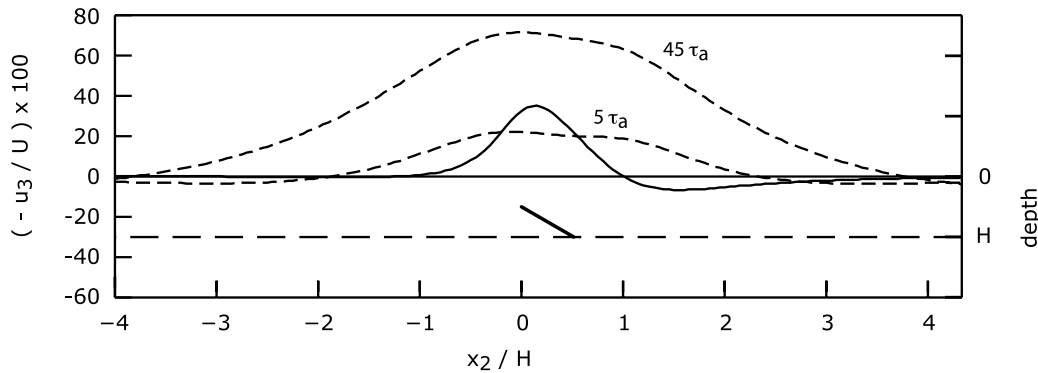
B. Thrust fault - Viscoelastic - Gravitational
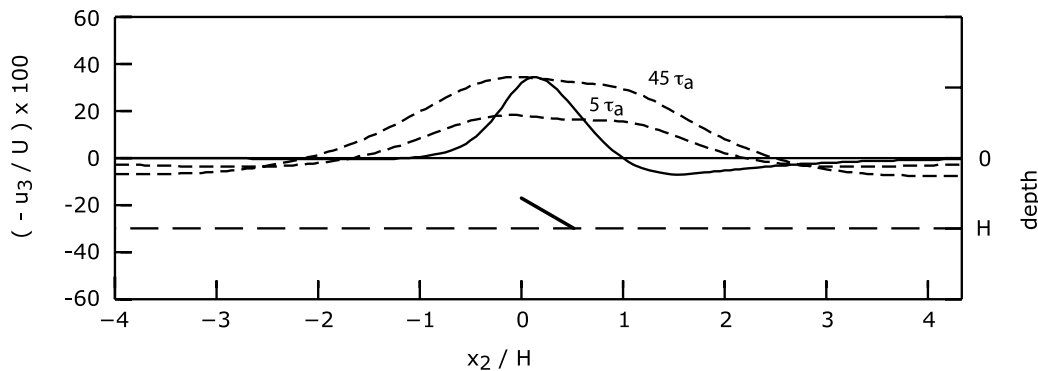
Figure 9. Effect of gravity on the post-seismic displacement following a thrust fault. The brittle–ductile transition occurs at depth H. The fault is $20H/3$ long in the strike direction, H wide in the dip direction and U is the magnitude of dip-slip. The fault tip is buried at $H/2$ and the fault plane dips $30°$. The coseismic vertical displacement is indicated by the solid profile. The dashed lines correspond to the post-seismic displacement. (a) The surface displacement after 5 and 45 relaxation times τ_a due to a linear viscous relaxation in the half-space below depth H. (B) the surface displacement after 5 and 45 relaxation times when surface buoyancy due to a density contrast at the surface is accounted for. The intensity of the gravitational restoring force is controlled by the dimensionless number $\Gamma H = 2.475 \times 10^{-2}$ corresponding to a Poisson's ratio $\nu = 1/4$, a density contrast $\Delta\rho = 3.3 \times 10^3 \, \mathrm{kg \, m^{-3}}$ and shear modulus $G = 30 \, \mathrm{GPa}$. The effect of surface buoyancy is to damp the large-wavelength components of vertical displacements. The simulations compare successfully with the results of (Rundle 1982, Figs 6 and 7) and (Pollitz 1997, Fig. 3).

incorporate realistic aspects of faulting including complex fault geometry, localization of deformation, gravitational effects and realistic variations of inelastic properties. Our semi-analytic approach simplifies the treatment of non-linear rheologies such as power-law creep and rate-strengthening friction and enables a possibility of studying interactions between multiple mechanisms in a self-consistent manner.

REFERENCES

Abramowitz, M. & Stegun, I., 1972. *Handbook of Mathematical Functions with Formulas, Graphs and Mathematical Tables,* 1046 pp., U.S. Government Printing Office, Washington, DC.

Backus, G. & Mulcahy, M., 1976. Moment tensors and other phenomenological descriptions of seismic sources–II. Discontinuous displacements, *Geophys. J. R. astr. Soc.,* **47,** 301–329.

Barbot, S. & Fialko, Y., 2010. Fourier-domain Green function for an elastic semi-infinite solid under gravity, with applications to earthquake and volcano deformation, *Geophys. J. Int.,* in press, doi:10.1111/j.1365-246X.2010.04655.x.

Barbot, S., Fialko, Y. & Sandwell, D., 2008a. Effect of a compliant fault zone on the inferred earthquake slip distribution, *J. geophys. Res.,* **113**(B6), doi:10.1029/2007JB005256.

Barbot, S., Hamiel, Y. & Fialko, Y., 2008b. Space geodetic investigation of the coseismic and postseismic deformation due to the 2003 Mw 7.2 Altai earthquake: implications for the local lithospheric rheology, *J. geophys. Res.,* **113,** B03403, doi:10.1029/2007JB005063.

Barbot, S., Fialko, Y. & Bock, Y., 2009a. Postseismic deformation due to the Mw 6.0 2004 Parkfield earthquake: stress-driven creep on a fault with spatially variable rate-and-state friction parameters, *J. geophys. Res.,* **114,** B07405, doi:10.1029/2008JB005748.

Barbot, S., Fialko, Y. & Sandwell, D., 2009b. Three-dimensional models of elasto-static deformation in heterogeneous media, with applications to the Eastern California Shear Zone, *Geophys. J. Int.,* **179**(1), 500–520.

Biggs, J., Burgmann, R., Freymueller, J.T., Lu, Z., Parsons, I.R.B., Schmalzle, G. & Wright, T., 2009. The postseismic response to the 2002 M 7.9 Denali fault earthquake: constraints from InSAR 20032005, *Geophys. J. Int.,* **176,** 353–367, 2009.

Biot, M.A., 1941. General theory of three-dimensional consolidation, *Appl. Phys.,* **12,** 155–164.

Brace, W.F. & Kohlstedt, D.L., 1980. Limits on lithospheric stress imposed by laboratory experiments, *J. geophys. Res.,* **85**(B11), 6248–6252.

Bredehoeft, J.D., 1967. Response of well-aquifer systems to earth tides, *J. geophys. Res.,* **72,** 3075–3087.

Bürgmann, R., Ergintav, S., Segall, P., Hearn, E.H., McClusky, S., Reilinger, R.E., Woith, H. & Zschau, J., 2002. Time-dependent distributed afterslip on and deep below the Izmit earthquake rupture, *Bul. seism. Soc. Am.,* **92**(1), 126–137.

Byerlee, J., 1978. Friction of rock, *Pure appl. Geophys.,* **116,** 615–626.

Cochran, Y., Li, Y.-G., Shearer, P., Barbot, S., Fialko, Y. & Vidale, J., 2009. Seismic and geodetic evidence for extensive, long-lived fault damage zones, *Geology,* **37**(4), 315–318.

Coussy, O., 2004. *Poromechanics,* John Wiley & Sons Ltd., Chichester, UK.

Deng, J., Gurnis, M., Kanamori, H. & Hauksson, E., 1998. Viscoelastic flow in the lower crust after the 1992 landers California, earthquake, *Science,* **282,** 1689–1692.

Detournay, E. & Cheng, A.H.-D., 1993. Fundamentals of poroelasticity, in *Comprehensive Rock Engineering: Principles, Practice and Projects,* Vol. 2, pp. 113–171, ed. Hudson, J.A., Pergamon Press, Oxford, UK.

Dieterich, J.H., 1979. Modeling of rock friction 1. experimental results and constitutive equations, *J. geophys. Res.,* **84**(B5), 2161–2168.

Dieterich, J.H., 1992. Earthquake nucleation on faults with rate- and state-dependent strength, *Tectonophysics,* **211,** 115–134.

Ergintav, S. *et al.,* 2009. Seven years of postseismic deformation following the 1999, M = 7.4 and M = 7.2, Izmit-Düzce, Turkey earthquake sequence, *J. geophys. Res.,* **114,** B07403, doi:10.1029/2008JB006021.

Fialko, Y., 2004. Evidence of fluid-filled upper crust from observations of post-seismic deformation due to the 1992 M_w7.3 Landers earthquake, *J. geophys. Res.,* **109,** B08401, doi:10.1029/2004JB002985.

Freed, A.M., 2007. Afterslip (and only afterslip) following the 2004 Parkfield, California, earthquake, *Geophys. Res. Lett.,* **34**, doi:10.1029/2006GL029155.

Freed, A.M. & Bürgmann, R., 2004. Evidence of power-law flow in the Mojave desert mantle, *Nature,* **430,** 548–551.

Freed, A.M., Bürgmann, R., Calais, E., Freymueller, J. & Hreinsdottir, S., 2006. Implications of deformation following the 2002 Denali, Alaska, earthquake for postseismic relaxation processes and lithospheric rheology, *J. geophys. Res.,* **111,** B01401, doi:10.1029/2005JB003894.

Freed, A.M., Bürgmann, R. & Herring, T., 2007. Far-reaching transient motions after Mojave earthquakes require broad mantle flow beneath a strong crust, *Geophys. Res. Lett.,* **34**(19), doi:10.1029/2007GL030959.

Heap, M.J., Baud, P., Meredith, P.G., Bell, A.F. & Main, I.G., 2009. Time-dependent brittle creep in Darley Dale sandstone, *J. geophys. Res.,* **114,** B07203, doi:10.1029/2008JB006212.

Hsu, Y.-J. *et al.,* 2006. Friction afterslip following the 2005 Nias-Simeulue earthquake, Sumatra, *Science,* **312,** 1921–1926.

Johnson, K.J., Burgmann, R. & Larson, K., 2006. Frictional properties on the San Andreas fault near Parkfield, California, inferred from models of afterslip following the 2004 earthquake, *Bull. seism. Soc. Am.,* **96**(4B), S321–S338.

Johnson, K.M., Bürgmann, R. & Freymueller, J.T., 2009. Coupled afterslip and viscoelastic flow following the 2002 Denali fault, Alaska earthquake, *Geophys. J. Int.,* **176**(3), 670–682.

Jonsson, S., Segall, P., Pedersen, R. & Bjornsson, G., 2003. Post-earthquake ground movements correlated to pore-pressure transients, *Nature,* **424,** 179–183.

Karato, S. & Wu, P., 1993. Rheology of the upper mantle: a synthesis, *Science,* **260,** 771–778.

Karato, S.-I., 2008. *Deformation of Earth Materials: An Introduction to the Rheology of Solid Earth,* Cambridge University Press, Cambridge.

Karato, S.-I., Paterson, M.S. & Fitzgerald, J.D., 1986. Rheology of synthetic olivine aggregates—influence of grain size and water, *J. geophys. Res.,* **91,** 8151–8176, doi:10.1029/JB091iB08p08151.

Kirby, S.H. & Kronenberg, A.K., 1987. Rheology of the lithosphere; selected topics., *Rev. Geophys.,* **25,** 1219–1244.

Kohlstedt, D.L., Evans, B. & Mackwell, S.J., 1995. Strength of the lithosphere: constraints imposed by laboratory experiments, *J. geophys. Res.,* **100,** 17 587–17 602.

Kumpel, H.-J., 1991. Poroelasticity: parameters reviewed, *Geophys. J. Int.,* **105,** 783–799.

Love, A.E.H., 1927. *A Treatise on the Mathematical Theory of Elasticity,* Cambridge University Press, Cambridge, reprinted in 1944 by Dover Publications, New York.

Malvern, L.E., 1969. *Introduction to the Mechanics of a Continuum Medium,* 713 pp., Prentice-Hall, Englewood Cliffs, NJ.

Marone, C., Scholz, C. & Bilham, R., 1991. On the mechanics of earthquake afterslip, *J. geophys. Res.,* **96,** 8441–8452.

Marone, C.J., 1998. Laboratory-derived friction laws and their application to seismic faulting, *Ann. Rev. Earth planet. Sci.,* **26,** 643–696.

Masterlark, T. & Wang, H.F., 2002. Transient stress-coupling between the 1992 Landers and 1999 Hector Mine, California, earthquakes, *Bull. seism. Soc. Am.,* **92**(4), 1470–1486, doi:10.1785/0120000905.

Nemat-Nasser, S., 2004. *Plasticity. A Treatise on Finite Deformation of Heterogeneous Inelastic Materials,* Cambridge Monographs on Mechanics, Cambridge University Press, Cambridge.

Nemat-Nasser, S. & Hori, M., 1999. *Micromechanics: Overall Properties of Heterogeneous Materials,* 2nd ed. , Elsevier, Amsterdam.

Nur, A. & Mavko, G., 1974. Postseismic viscoelastic rebound, *Science,* **183,** 204–206.

Parsons, T., 2005. Tectonic stress in California modeled from GPS observations, *J. geophys Res.,* **111,** B03407, doi:10.1029/2005JB003946.

Pearse, J. & Fialko, Y., 2010. Mechanics of active magmatic intraplating in the Rio Grande Rift near Socorro, New Mexico, *J. geophys. Res.,* in press, doi:10.1029/2009JB006592.

Peltzer, G., Rosen, P., Rogez, F. & Hudnut, K., 1998. Poro-elastic rebound along the landers 1992 earthquake surface rupture, *J. geophys. Res.,* **103**(B12), 30 131–30 145.

Perfettini, H. & Avouac, J.-P., 2004. Postseismic relaxation driven by brittle creep: a possible mechanism to reconcile geodetic measurements and the decay rate of aftershocks, application to the Chi-Chi earthquake, Taiwan, *J. geophys. Res.,* **109,** B02304, doi:10.1029/2003JB002488.

Perfettini, H. & Avouac, J.-P., 2007. Modeling afterslip and aftershocks following the 1992 Landers earthquake, *J. geophys. Res.,* **112**(B07409).

Pollitz, F.F., 1997. Gravitational viscoelastic postseismic relaxation on a layered spherical Earth, *J. geophys. Res.,* **102,** 17 921–17 941.

Pollitz, F.F., Peltzer, G. & Bürgmann, R., 2000. Mobility of continental mantle: evidence from postseismic geodetic observations following the 1992 landers earthquake, *J. geophys. Res.,* **105**(B4), 8035–8054.

Press, W.H., Teukolsky, S.A., Vetterling, W.T. & Flannery, B.P., 1992. *Numerical Recipes in C: The Art of Scientific Computing,* 2nd ed., 994 pp., Cambridge University Press, New York.

Reches, Z., Schubert, G. & Anderson, C., 1994. Modeling of periodic great earthquakes on the San Andreas fault: effects of nonlinear crustal rheology, *J. geophys. Res.,* **99,** 21 983–22 000.

Reilinger, R., 1986. Evidence for postseismic viscoelastic relaxation following the 1959 M = 7.5 Hebgen Lake, Montana, earthquake, *J. geophys. Res.,* **91**(B9), 9488–9494.

Rice, J.R. & Cleary, M.P., 1976. Some basic stress-diffusion solutions for fluid-saturated elastic porous media with compressible constituents, *Rev. Geophys.,* **14,** 227–241.

Rice, J.R., Lapusta, N. & Ranjith, K., 2001. Rate and state dependent friction and the stability of sliding between elastically deformable solids, *J. Mech. Phys. Solids,* **49,** 1865–1898.

Rudnicki, J.W., 1985. Effect of pore fluid diffusion on deformation and failure of rock, in *Mechanics of Geomaterials - Rocks, Concretes, Soils,* pp. 315–347, ed. Bazant, Z.P., Wiley, Chichester.

Rudnicki, J.W., 1986. Fluid mass sources and point forces in linear elastic diffusive solids, *Mech Mat.,* **5,** 383–393.

Rundle, J.B., 1982. Viscoelastic-gravitational deformation by a rectangular thrust fault in a layered earth, *J. geophys. Res.,* **87**(B9), 7787–7796.

Savage, J., 2000. Viscoelastic-coupling model for the earthquake cycle driven from below, *J. geophys. Res.,* **105**(B11), 25 525–25 532.

Scholz, C.H., 1988. The brittle-plastic transition and the depth of seismic faulting, *Geologische Rundschau,* **77**(1), 319–328.

Scholz, C.H., 1998. Earthquakes and friction laws, *Nature,* **391,** 37–42.

Segall, P., 1985. Stress and subsidence resulting from subsurface fluid withdrawal in the epicentral region of the 1983 Coalinga earthquake, *J. geophys. Res.,* **90**(B8), 6801–6816.

Segall, P., 1989. Earthquakes triggered by fluid extraction, *Geology,* **17,** 942–046.

Singh, S.J., Rani, S. & Kumar, R., 2007. Quasi-static deformation of a poroelastic half-space with anisotropic permeability by two-dimensional surface loads, *Geophys. J. Int.,* **170**(3), 1311–1327.

Smith, B. & Sandwell, D., 2004. A three-dimensional semianalytic viscoelastic model for time-dependent analyses of the earthquake cycle, *J. geophys. Res.,* **109,** B12401, doi:10.1029/2004JB003185.

Tse, S.T. & Rice, J.R., 1986. Crustal earthquake instability in relation to the depth variation of frictional slip properties, *J. geophys. Res.,* **91**(B9), 9452–9472.

Wang, H.F., 2000. *Theory of Linear Poroelasticity with Applications to Geomechanics & Hydrogeology,* Princeton University Press, Princeton, NJ.

Weertman, J. & Weertman, J.R., 1975. High temperature creep of rock and mantle viscosity, *Ann. Rev. Earth planet. Sci.,* **3,** 293–315, doi:10.1146/annurev.ea.03.050175.001453.

APPENDIX A: CONTINUUM THEORY OF POROELASTIC REBOUND

In this Appendix, we show that the poroelastic rebound problem, which involves the pore fluid diffusion and the coupled elastic deformation following an initial stress perturbation, can be presented as a generalized viscoelastic relaxation whereby some inelastic strain accumulates to relax a physical quantity in the material. In a poroelastic composite the relaxed quantity is the isotropic stress as opposed to, for example, the deviatoric stress in a Maxwellian viscoelastic body. In this framework, poroelasticity is an analogue of macroscopic bulk viscosity. The appendix is organized as follows. First, we present the basic equations of linear poroelasticity (Bredehoeft 1967; Rice & Cleary 1976; Rudnicki 1985; Kumpel 1991) along with the respective constitutive relations and conservations laws. Next, we show that the governing equations of poroelasticity can be written using two end-member representations. The classic formulation uses the pore pressure as dynamic variable and the elastic moduli for drained condition as model parameters. An alternative approach uses the perturbation in fluid density in the pore space as a dynamic variable and the elastic moduli for undrained condition to parameterize the pore fluid flow and the associated elastic deformation. The proposed formulation is compatible with a general viscoelastoplastic behaviour of the crust and allows the modelling of complete time-series of a poroelastic rebound.

A1 The classic theory of poroelasticity

Hereafter we adopt the nomenclature of Kumpel (1991) and Wang (2000). In a poroelastic composite material, a linearized equation of state relates a relative change in fluid content

$$\zeta = \frac{m_f - m_{f_0}}{\rho_0}, \tag{A1}$$

where $m_f - m_{f_0}$ denotes the increment of fluid mass per unit rock volume and ρ_0 is a reference density of the pore fluid, to the given pore pressure and confining stress as follows (Biot 1941; Rice & Cleary 1976)

$$\zeta = \frac{\alpha}{\kappa_d} \left(p/B + \frac{\sigma_{kk}}{3} \right), \tag{A2}$$

Table A1. Notations.

α	poroelastic coefficient of effective stress
$a\sigma$	fault friction parameter
β	poroelastic coupling coefficient
ϵ_{ij}	total strain tensor
ϵ_{ij}^e	elastic strain
ϵ_{ij}^i	inelastic strain
ζ	fluid content in pore space
B	Skempton's coefficient
C_{ijkl}	elastic tensor
D	fluid content diffusivity
D_{ijkl}	compliance tensor
f_i	equivalent body force
G	elastic shear modulus
G_{ij}	elastic Green's function
$\dot{\gamma}$	strain rate (scalar)
γ	cumulative strain
Γ	buoyancy critical wavenumber
κ	bulk modulus
M	Biot's coefficient
$\dot{m}_{ij}$	power density tensor
m_f	fluid mass per unit rock volume
ν	Poisson's ratio
η	viscosity
$\hat{n}_i$	half-space normal vector
p	pore pressure
R_{ij}	strain-rate direction
ρ_0	reference density of pore fluid
$\Delta\rho$	surface density contrast
σ	macroscopic confining stress
σ_{ij}	macroscopic stress tensor
$\dot{s}_0$	reference fault creep rate
t_i	surface traction
τ	shear stress
u_i	displacement vector
v_i	velocity vector
χ	Darcy's conductivity

where B is the Skempton coefficient, κ_d is the bulk modulus of the composite for drained condition and α is the dimensionless coefficient of effective stress (Table A1). The pore pressure p is positive for compression and the confining stress in the solid matrix $\sigma = \sigma_{kk}/3$ is positive for extension. Eq. (A2) is a linearized equation of state for the fluid density. The stress–strain relation for the composite material is described by the generalized Hooke's law which is extended for poroelastic composite materials

$$\sigma_{ij} = 2G \frac{\nu_d}{1 - 2\nu_d} \epsilon_{kk} \delta_{ij} + 2G\epsilon_{ij} - \alpha p \delta_{ij}, \tag{A3}$$

where G is the shear modulus, ν_d is the Poisson's ratio for drained condition and the ϵ_{ij} are the macroscopic strain components. In particular, summing diagonal terms in eq. (A3), one has

$$\sigma = \kappa_d \epsilon_{kk} - \alpha p. \tag{A4}$$

For vanishing pore pressure ($p = 0$), one obtains a form of Hooke's law where the drained elastic moduli appear as model parameters.

The fluid diffusion law is obtained from the conservation of fluid mass, $\dot{m}_f + \rho_0 q_{k,k} = 0$, with a Darcy flow law $q_i = -\chi p_{,i}$ for the flux q_i, giving rise to

$$\dot{\zeta} = \chi p_{,kk}, \tag{A5}$$

where χ is the Darcy conductivity in units of length^3 × time × mass^{-1}. The Darcy conductivity is the ratio of the rock permeability to the fluid viscosity $\chi = k/\mu_f$, assumed to be constant in eq. (A5). The permeability has the units $k \sim$ length^2 and the pore fluid

viscosity $\mu_f \sim$ mass $\times$ length^{-1} $\times$ time^{-1}. Some more complicated expressions of the pore fluid flow can include the effect of water head (e.g. Bredehoeft 1967) and/or anisotropic diffusivity (Singh *et al.* 2007).

A combination of constitutive relations (A2) and (A3) with the flow law (A5) together with the conservation of momentum equation $\sigma_{ij,j} = 0$ gives rise to a set of coupled governing equations that describes the evolution of the macroscopic displacement u_i and the pore pressure p of an isotropic and homogeneous porous medium. The coupled governing equations are (e.g. Kumpel 1991)

$$G\left(\frac{1}{1-2\nu_d}u_{k,ki} + u_{i,kk}\right) = \alpha p_{,i}, \tag{A6}$$

$$Q^{-1}\dot{p} = \chi p_{,kk} - \alpha \dot{u}_{k,k}, \tag{A7}$$

where Q^{-1} is a compressibility. The parabolic eq. (A7) is subject to the boundary condition $p = 0$ at the surface of the half-space. Parameters α and Q^{-1} can be expressed in terms of the Poisson's ratio for undrained conditions ν_u and the Skempton ratio B as follows:

$$\alpha = \frac{3(\nu_u - \nu_d)}{(1 - 2\nu_d)(1 + \nu_u)B} \tag{A8}$$

and

$$Q^{-1} = \frac{3}{2}\frac{1 - 2\nu_u}{1 + \nu_u}\frac{\alpha}{GB} = \frac{\alpha}{\kappa_u B}. \tag{A9}$$

The pore pressure p appears as a forcing term in the Navier's equation (A6) and the matrix dilatation $u_{k,k}$ is a forcing term of the diffusion equation (A7), giving rise to a fully coupled system.

A2 A bulk-viscosity formulation for poroelasticity

We now draw a parallel between the classic poroelastic theory and the viscoelastic formalism presented in Section 3. We show that the classic governing equations of poroelasticity can be written using the effective change in fluid density in the pore volume and the elastic moduli for undrained condition to parameterize the pore fluid flow and the associated elastic deformation. Our proposed formulation can be viewed as a macroscopic formulation, where only two additional parameters, a coupling coefficient β and a diffusivity D, compared to linear elasticity, are required to describe the time-dependent deformation. We show how these parameters relate to the microscopic properties of the fluid-solid composite.

First, to simplify the poroelastic equations, we define the effective coupling coefficient

$$\beta = B\alpha. \tag{A10}$$

We define the dynamic variables as the effective change of pore fluid density,

$$\gamma = B\frac{m_f - m_{f_0}}{\rho_0}. \tag{A11}$$

By definition, the inelastic deformation γ is identically zero in undrained condition. The linearized equation of state for the pore fluid can now be written

$$\gamma = \frac{\beta}{\kappa_d}\left(p/B + \frac{\sigma_{kk}}{3}\right). \tag{A12}$$

Using eq. (A10) and the stress–strain relation (A3) for the composite material we obtain the following relationship for the spherical part of the stress tensor,

$$\frac{\sigma_{kk}}{3} = \kappa_d \epsilon_{kk} - \beta p/B. \tag{A13}$$

Combining eqs (A10), (A12) and Biot's stress–strain eq. (A4) we obtain an alternative isotropic strain-rate relation using a new dynamic variable γ,

$$\frac{\sigma_{kk}}{3} = \frac{K_d}{1-\beta}(\epsilon_{kk} - \gamma) \tag{A14}$$

Setting $\gamma = 0$, we obtain the following links between drained and undrained moduli

$$\begin{aligned}\kappa_u &= \frac{1}{1-\beta}\kappa_d,\\\lambda_u &= \frac{2G}{3}\frac{1}{1-\beta}\left(\beta + \frac{3\nu_d}{1-2\nu_d}\right),\\\nu_u &= \frac{3\nu_d + \beta(1-2\nu_d)}{3-\beta(1-2\nu_d)},\end{aligned} \tag{A15}$$

where κ_u, λ_u and ν_u, respectively, are the bulk modulus, the Lamé parameter and the Poisson's ratio, respectively, for undrained condition. Reciprocally, given undrained elastic moduli and an effective coupling coefficient, one has

$$\begin{aligned}\lambda_d &= (1-\beta)\lambda_u - \beta\frac{2G}{3},\\\nu_d &= \frac{\beta(1+\nu_u) - 3\nu_u}{2\beta(1+\nu_u) - 3}.\end{aligned} \tag{A16}$$

The second and third formulas in eqs (A15) and (A16) are simply derived from the first one using well-known relations between isotropic elastic moduli (e.g. Malvern 1969). The isotropic stress in the solid matrix can be written

$$\frac{\sigma_{kk}}{3} = K_u(\epsilon_{kk} - \gamma), \tag{A17}$$

which is the counterpart of eq. (A13) that employs the effective pore pressure instead of fluid content as a dynamic variable. Alternatively, the coupling coefficient β can be retrieved from the inferred values of drained and undrained moduli

$$\beta = 1 - \frac{K_d}{K_u} = 3\frac{\nu_u - \nu_d}{(1-2\nu_d)(1+\nu_u)}, \tag{A18}$$

where the effective bulk modulus in undrained (initial) condition K_u is greater than in drained condition, at full relaxation ($K_u \geq K_d$). Similarly, drained and undrained conditions are associated with effective drained ν_d and undrained ν_u Poisson's ratios, respectively, such that $\nu_u \geq \nu_d$.

Combining eqs (A12) and (A17), we obtain an expression for the pore pressure in terms of volume changes in the solid matrix and the pore fluid,

$$\alpha p = \kappa_u(\gamma - \beta\epsilon_{kk}). \tag{A19}$$

Substituting eq. (A19) into Eq. (A3), we obtain the generalized stress–strain relation (see also Segall 1985,1989; Rudnicki 1986)

$$\sigma_{ij} = \lambda_u \epsilon_{kk}\delta_{ij} + 2G\epsilon_{ij} - \kappa_u\gamma\,\delta_{ij}, \tag{A20}$$

where the effective stress in the poroelastic composite is parameterized with the fluid dilatancy γ unlike in Biot's formulation that employs the pore pressure. Notice that eq. (A20) can be written

$$\sigma_{ij} = C_{ijkl}\left(\epsilon_{kl} - \frac{1}{3}\gamma\,\delta_{kl}\right) \tag{A21}$$

with the isotropic elastic stiffness tensor

$$C_{ijkl} = \lambda_u\,\delta_{ij}\delta_{kl} + G(\delta_{ij}\delta_{kl} + \delta_{ik}\delta_{jl}), \tag{A22}$$

which corresponds to our formulation for stress in a viscoelastic material with bulk viscosity, whereby ϵ_{kl} is the total strain,

$\epsilon_{kl}^i = \gamma \, \delta_{kl}/3$ is the inelastic strain and the isotropic elastic tensor C_{ijkl} is for undrained condition. Combining eqs (A5), (A17) and (A19) the Darcy's equation for fluid diffusion becomes

$$\dot{\gamma} = D \left[(1 - \beta)\gamma - \beta \frac{\sigma}{\kappa_u} \right]_{,jj} \tag{A23}$$

and the boundary condition $p = 0$ at the surface of the half-space becomes

$$\gamma = \frac{\beta}{1 - \beta} \frac{\sigma}{\kappa_u}, \qquad x_3 = 0, \quad t > 0. \tag{A24}$$

The diffusivity D, in units of length$^2 \times$ time^{-1}, a combination of the microscopic parameters, is given by

$$D = \kappa_u \frac{Bx}{\alpha} = Mx, \tag{A25}$$

where M is the Biot's modulus, the reciprocal of a storage coefficient (Detournay & Cheng 1993; Wang 2000). The parabolic eq. (A23) is compatible with the general form of a viscoelastic constitutive relation with work-hardening $\dot{\gamma} = f(\sigma_{ij}, \gamma)$. Poroelasticity is therefore an example of bulk viscosity and in this framework the coupling parameter β can be thought of as a work-hardening parameter.

Finally, using conservation of momentum with formulation (A20) one obtains the coupled governing equations

$$G \left[\frac{1}{1 - 2\nu_u} u_{k,ki} + u_{i,kk} \right] = \kappa_u \gamma_{,i},$$

$$\dot{\gamma} = D \left[(1 - \beta)\gamma - \beta \frac{\sigma}{\kappa_u} \right]_{,jj}, \tag{A26}$$

where only two additional model parameters are required to describe a poroelastic rebound compared to linear elasticity. Formulations (A6), (A7) and (A26) of the governing equations of poroelasticity are equivalent. Coupled eqs (A6) and (A7) make use of the pore pressure p and the drained elastic moduli to parameterize the time-dependent deformation, as suggested by Biot (1941), whereas eq. (A26) uses the effective fluid density change γ and the undrained elastic moduli.

One corollary from the presented analysis is that models of a poroelastic rebound from geodetic measurements can at best constrain two macroscopic parameters (e.g. our proposed parameters D and β). Inferences on microscopic parameters α, B and χ can only be attained with additional *in situ* measurements.